



저작자표시-변경금지 2.0 대한민국

이용자는 아래의 조건을 따르는 경우에 한하여 자유롭게

- 이 저작물을 복제, 배포, 전송, 전시, 공연 및 방송할 수 있습니다.
- 이 저작물을 영리 목적으로 이용할 수 있습니다.

다음과 같은 조건을 따라야 합니다:



저작자표시. 귀하는 원저작자를 표시하여야 합니다.



변경금지. 귀하는 이 저작물을 개작, 변형 또는 가공할 수 없습니다.

- 귀하는, 이 저작물의 재이용이나 배포의 경우, 이 저작물에 적용된 이용허락조건을 명확하게 나타내어야 합니다.
- 저작권자로부터 별도의 허가를 받으면 이러한 조건들은 적용되지 않습니다.

저작권법에 따른 이용자의 권리는 위의 내용에 의하여 영향을 받지 않습니다.

이것은 [이용허락규약\(Legal Code\)](#)을 이해하기 쉽게 요약한 것입니다.

[Disclaimer](#)

공학석사 학위논문

Synthesis and Characterization of Imidazole-based Organic-Inorganic Perovskites

이미다졸 기반의 유무기 페로브스카이트의
합성 및 특성 평가

2014년 1월

서울대학교 대학원

재료공학부

황진연

Synthesis and Characterization of Imidazole-based Organic-Inorganic Perovskites

지도 교수 남 기 태

이 논문을 공학 석사 학위 논문으로 제출함
2014년 1월

서울대학교 대학원
재료공학부
황 진 연

황 진 연 의 석사 학위 논문을 인준함

2014년 1월

위 원 장 홍 성 현 (인)
부위원장 남 기 태 (인)
위 원 장 호 원 (인)

ABSTRACT

Synthesis and Characterization of Imidazole-based Organic-Inorganic Perovskites

Jinyeon Hwang

Department of Materials Science and Engineering

The Graduate School
Seoul National University

Organic-inorganic perovskites (OIPs) are hybrid materials which contain cationic organic molecules in the lattice. Compared to conventional perovskites, solution-based processing is possible for OIPs to coat on various substrates easily with low cost. Nowadays, OIPs are receiving extensive attention because of its high efficiency as photosensitizer in solid-state solar cells.

However, most of researches related with OIPs photosensitizer are only focused on methyl ammonium lead iodide (MPI) which possesses short alkyl chain with primary amine. In other words, there are only limited variables that can change its properties. This makes further improvements of MPI difficult. Moreover, MPI has low stability under high humidity.

Here, we successfully synthesized new imidazole-based OIPs using biomolecules, histidine and histamine. In addition, we confirmed that our new perovskites can be applied as photosensitizer in solid-state solar cells. For materials characterization, single crystal structure analysis, band structure analysis, and thermal stability test were conducted. As a result, we verified

detailed crystallographic structure, and band position. To optimize the solar cell properties, we also optimized conditions with one-step spin-coating and two-step dip coating.

This research has three major impacts. First of all, we show the possibility that not only the primary amine, but also the whole imidazole group can be involved in inorganic layer. It is worth noting that the tuning of OIPs properties is possible by different types of organic molecules and functional groups. Secondly, we suggest the new point of convergence with biomolecules and inorganic materials through synthesized new hybrid materials. Thirdly, we confirm that our OIPs are relatively enduring in humid conditions than MPI. Successful improvement on water-resistance, however, is an essential requirement for the commercialization of OIPs-based solid-state solar cells.

Keywords: Organic-inorganic perovskites, Solid-state solar cells, Photosensitizer, Imidazole, Histidine, Histamine, Single crystal structure analysis, Band structure analysis, One-step spin-coating, Two-step dip-coating, Stability

Student Number: 2012 - 20644

CONTENTS

Abstract	i
Contents	iii
List of Tables	vi
List of Figures	vii

Chapter 1. Introduction

1.1	Organic-inorganic perovskites (OIPs)	1
1.1.1	Principles of organic-inorganic perovskites	3
1.1.2	Tolerance factor	8
1.2	Solid-state dye perovskite solar cells	14
1.2.1	Structure and mechanism	16
1.2.2	Current research on perovskites photosensitizer.....	20
1.3	Imidazole-based materials	27
1.4	Research scope and design	28
1.4.1	The bottleneck of (CH ₃ NH ₃)PbI ₃ photosensitizer	28
1.4.2	Advantages of imidazole-based OIPs photosensitizer	31

Chapter 2. Experimental and Procedure

2.1	Imidazole-based organic-inorganic perovskites	35
2.1.1	Materials	35
2.1.2	Synthesis of imidazolium iodide precursors	35
2.1.3	Synthesis of imidazole-based OIPs.....	37

2.1.4	Single crystal preparation	37
2.2	Solar cells fabrication	38
2.2.1	Fabrication methods.....	38
2.2.2	Coating techniques of OIPs photosensitizer	40
2.2.2.1	One-step spin-coating	
2.2.2.2	Two-step dip-coating	
2.3	Characterization	41
2.3.1	Scanning electron microscopy (SEM)	41
2.3.2	X-ray diffraction	42
2.3.2.1	Powder, Film X-ray diffraction	
2.3.2.2	Single crystal X-ray diffraction and synchrotron	
2.3.3	Thermogravimetry (TGA)	43
2.3.4	Band structure	43
2.3.4.1	Reflectance and Absorbance measurement	
2.3.4.2	Ultraviolet photoelectron spectroscopy (UPS)	
2.3.5	Photocurrent measurement.....	44
2.3.6	Photovoltaics measurement	45

Chapter 3. Results and Discussions

3.1	Structures and properties characterization	49
3.1.1	Crystal structure determination.....	49
3.1.1.1	Analysis of as-synthesized OIPs powder	
3.1.1.2	Computational analysis of single crystal	
3.1.2	Optical properties characterization	63
3.1.3	Band gap energy and band position determination	64
3.1.4	Thermal stability characterization.....	66

3.2	Coating dependence and optimization	73
3.2.1	One-step coating	73
3.2.1.1	Concentration dependence	
3.2.1.2	Organic solvent dependence	
3.2.1.3	Pre-treatment dependence	
3.2.2	Two-step coating	80
3.2.2.1	PbI ₂ coating dependence	
3.2.2.2	Concentration of imidazolium iodide dependence	
3.2.2.3	Dipping time dependence	
3.3	Photovoltaic characterization	88
3.3.1	Photoactivity determination and screening	88
3.3.2	Band analysis for solid-state solar cells	89
3.3.3	I-V spectra analysis	90
3.3.3.1	One-step coated cells optimization	
3.3.3.2	Two-step coated cells optimization	
3.3.3.3	Long term stability test	
<hr/>		
	Chapter 4. Conclusion.....	104
<hr/>		
	References	107
<hr/>		
	국문초록	117
	Acknowledgements	119
<hr/>		

List of Tables

Table 1.	Crystal data of hPI compared to hPBr	61
Table 2.	Selected bond distances (\AA) and bond angles ($^\circ$) of hPI.....	62
Table 3.	Photovoltaic parameters of two-step hPI solid- state solar cells	100
Table 4.	Photovoltaic parameters of two-step hPI solid- state solar cells	101

List of Figures

- Figure 1.1** General crystal structures of metal halide perovskites (ABX_3).....10
- Figure 1.2** (a) Halogen bonding between plugged-in ammonium cation and inorganic layer (b) Structural difference depending on the number of amine in alkyl chain..... 11
- Figure 1.3** Different structures of 2-dimensional OIPs12
- Figure 1.4** (a) Halide ion dependence of $(C_5H_4CH_2NH_3)_2PbX_4$ OIPs (b) Organic chain dependence of $(C_4H_9NH_3)_2(CH_3NH_3)_{n-1}Sn_nI_{3n+1}$ OIPs.....13
- Figure 1.5** Schematic structure of solid-state solar cells....23
- Figure 1.6** I-V curve analysis to get J_{sc} , V_{oc} , fill factor, and efficiency.....24
- Figure 1.7** The first report of OIPs-based solid-state solar cells25
- Figure 1.8** World-recording cell efficiencies in solar cell industry.....26
- Figure 1.9** (a) Different types of nitrogen-involved hetero-

	atom aromatic rings (b) Chemical structure and molecular weight of histidine and histamine	34
Figure 2.1	Schematic of (a) imidazolium iodide synthesis and (b) OIPs synthesis	46
Figure 2.2	Various methods of single crystal preparation in solution.....	47
Figure 2.3	Schematic of solid-state perovskite cells fabrication (a) one-step coating, (b) two-step coating.....	48
Figure 3.1	SEM images of (a), (d) PbI_2 , (b), (e) HPI and (c), (f) hPI crystal	56
Figure 3.2	Powder XRD pattern of PbI_2 precursor, HPI, and hPI	57
Figure 3.3	Images of hPI single crystal structure along (a) (100)-direction, and (b) (001)-direction	58
Figure 3.4	Halogen bonds between protonated histamine and iodides in PbI_6 octahedrons.....	59
Figure 3.5	Corrugated structure of PbI_6 octahedron chain with I7-I8 corner-sharing.	60
Figure 3.6	(a) Diffuse mode reflectance plot of HPI and hPI	

	(b) Absorption spectra of HPI and hPI	68
Figure 3.7	Kubelka-Munk diagrams of (a) HPI and (b) hPI for determination of band gap energy	69
Figure 3.8	UPS spectra of (a) HPI and (b) hPI.....	70
Figure 3.9	Schematic band structure of PbI ₂ , MPI, HPI, and hPI	71
Figure 3.10	TGA data of (a) HPI and (b) hPI.....	72
Figure 3.11	hPI thickness variations depending on the concentration.....	78
Figure 3.12	SEM images of one-step spin-coated hPI film depending on types of organic solvent and pre-treatments	79
Figure 3.13	(a) Section SEM image of PbI ₂ coating, (b) dependence of thickness on PbI ₂ concentration, two-step coated (c) HPI (d) hPI film XRD data depending on PbI ₂ concentration	85
Figure 3.14	Two-step (a) HPI and (b) hPI film XRD data depending on the concentration of imidazolium iodide from 10 mM to 50 mM	86
Figure 3.15	Two-step (a) HPI and (b) hPI film XRD data	

depending on the dipping time.....	87
Figure 3.16 Photocurrent generation from hPI perovskite...	96
Figure 3.17 Schematic band alignment for solid-state solar cells with structure	97
Figure 3.18 Optimization of one-step hPI cells based on I-V analysis.....	98
Figure 3.19 Efficiency comparisons among one-step hPI cell, two-step hPI cell, and MPI cell.....	99
Figure 3.20 Long term stability of hPI perovskite coating on FTO glass	102
Figure 3.21 Cell stability plots of hPI perovskite cells by comparing J_{SC} , V_{OC} , fill factor, and efficiency for 120 hours.....	103

Chapter 1. Introduction

1.1 Organic-inorganic perovskites (OIPs)

Hybrid materials have been attracting enormous interests from many scientists because of their outstanding physical and chemical properties like a single material.¹ (collaborative properties) For instance, peptide-inorganic hybrids let seashells to have high mechanical strength.² Furthermore, chemical silanization of organic molecules allow materials to acquire an unique stability and inertness.³ In the case of metal-organic frameworks, (MOFs) there are many nano-sized pores generated by the interactions between metal ion and organic ligand. These pores are enough in number to contain hydrogen molecules, so that engineers use MOFs hybrids as hydrogen storage materials.⁴ Organic-inorganic perovskites (OIPs) are also a good example of hybrid materials. OIPs contain not only metal ions, but also organic molecules in a lattice. In this research, we focused on OIPs in particular among many hybrid materials because of its uniqueness.

Perovskites is well-known crystal structures whose chemical formula is ABX_3 .⁵ (Figure 1.1) Ion A takes position in the center of the lattice, ((0,0,0) position) ion B locates at corner, ((1/2, 1/2, 1/2) position) and X ions are face-centered of the lattice. ((1/2, 1/2, 0) position) For charge neutralization, both ion A and ion B are cation, and X is anion. Each A and B has very different sizes, with the ionic radius of A generally bigger than that of B.⁶ On the other hand, many of X ions are bonded with those cations. As a result, net charge of

the whole structure is equal to zero. By doping or substitution, the chemical formula of perovskites can be changed,⁷ and it can also cause lattice distortion. Metal oxides are in most of inorganic materials that have perovskites structures, such as BaTiO₃, SrTiO₃ perovskites. Interestingly, because of the bulky volume of A ion, A cation vibrates along the c-axis. This phenomenon generates an ion shift: polarized positive charges are generated. Ion shift makes perovskites have characteristic properties including ferroelectricity and superconductivity.⁸

In 1884, H. Topsoe reported very interesting hybrid materials.⁹ There was a first attempt to substitute cation in A sites where bulky cations are located. Instead of classical metal ions, Topsoe tried to put positively charged organic molecules which contains alkyl ammonium group. Successfully, these synthesized organic hybridized materials were reported as organic-inorganic perovskites. (OIPs) The first trial of OIPs synthesis made new research field. When organic cation involves into metal halide compounds, organic materials are located in A site, while metal ions are in B, and halide anions are in X position.¹⁰ In fact, organic compound participates in the lattice to form crystals. A series of corner-sharing octahedron metal halides are surrounds these organic-inorganic cations. Nowadays, OIPs attracts a lot of interests in that these materials have a unique structure hybridized with organic materials. Inorganic parts offer high mechanical strength, thermal stability, and optoelectronic properties. On the other hand organic parts help easy processing, solution-based processing, and optoelectronic enhancement.

1.1.1 Principles of organic-inorganic perovskites

The mechanism of OIPs formation is simple. Protonated amine group has a positive charge of +1. For neutralizing the charge of the whole structure, +2 cationic divalent ion and -1 halide ion cooperate to make the net charge zero. This is the ABX_3 structure. In detail, organic chain is electrostatically bounded with inorganic perovskites layer. Therefore, the valence of metal ion should be +2. Additionally, one of the most important interaction factors is the halogen bonding between the hydrogen in ammonium and surrounded halides ions. Because halogen bonding is one of the strongest among intermolecular forces,¹¹ it helps stabilize OIPs to maintain its unique structure. (Figure 1.1)

There are two different structures in OIPs. One is that 3-dimensional perovskites. Small enough organic molecules fully involve in the crystal lattice. (ABX_3) In contrast, if the length of the organic chain is longer, it may be bigger than the limited A site in perovskites structures. In this case, the structure cannot be formed. However, non-cooperative parts in the long alkyl chain can be dangling outside from the inorganic layer. These dangling side chains are packed in order through intermolecular van der Waals force. In other words, organic molecules are stacked in the interlayer space between inorganic layers. This layer-by-layer perovskites are called 2-dimensional OIPs. (A_2BX_4 , or ABX_4) Whether certain perovskites has a 3D structure or 2D structure depends on the tolerance factor.¹² Mathematical formulae and calculation methods of the tolerance factor are introduced in chapter 1.1.2 in detail.

In figure 1.2, we summarized various types of 2-dimensional OIPs structures. 2-dimensional perovskites can be classified into three types: $\langle 100 \rangle$ -oriented, $\langle 110 \rangle$ -oriented, and $\langle 111 \rangle$ -oriented.¹³ In OIPs, there is a special limitation of the A site. Therefore, a small size of the organic part can be penetrated into inorganic octahedrons. In this paper, we will call this interacting group as a plugging-in group. The plugging-in group can penetrate into inorganic octahedrons to make interactions. Generally, the ammonium cation at the end of alkyl chain interacts and combines with inorganic parts in OIPs.

$\langle 100 \rangle$ -oriented layer OIPs is a well-known structure for 2-dimensional perovskites. The plugging-in groups are aligned along the $\langle 100 \rangle$ direction of the cell, and makes interaction. Around this organic ordering, monolayer of inorganic layers is sandwiched between upper and lower layers of organic cations. Similarly, $\langle 110 \rangle$ and $\langle 111 \rangle$ oriented cell has favoring packing direction along $\langle 110 \rangle$, $\langle 111 \rangle$ to make layer-by-layer structure. However, $\langle 110 \rangle$ and $\langle 111 \rangle$ OIPs have been rarely reported.^{14, 15} In detail, the structure of $\langle 110 \rangle$ -oriented OIPs has zigzag networks of inorganic layers. Otherwise, $\langle 111 \rangle$ -oriented OIPs has an isolated inorganic octahedron. (quasi-0-dimensional perovskites) Both of them are thermodynamically unstable without any confinement by binding with rigid organic chains.

The number of amines in organic molecules also affects the chemical formula and structure of 2-dimensional OIPs. If there is only one amine, the number of possible plugging-in group will be only one. As a result, other side chains all aligned at the interlayer space.^{16, 17} At this time, the chemical

formula is expressed as A_2BX_4 . On the other hand, if there is more than one additional amine, or in the case of dicationic diamine molecules, plugging-in groups will be more than two which makes bindings with both upper and lower inorganic layers.¹⁸ In this case, the chemical formula is ABX_4 . The left alkyl chain between two amines is extended to pack as an organic layer. Diamine has higher confinement effects induced by organic carbon chains than mono-amine materials. (Figure 1.2)

Synthetic OIPs have many advantages. First of all, (1) they provide ideal opportunities to integrate different types of materials because they are organic-inorganic hybrid materials. Unlike randomly combined other hybrid materials, OIPs have long-range ordering to align organic molecules. (2) In addition, solution-based processing is possible in OIPs systems. Therefore, they are easy to coat on various substrates (glass, silicon, flexible polymer), and simple to fabricate thin-film structure.¹⁹ Additionally, the coating techniques are performed under mild conditions without heat stress. As a result, they are compatible in a wide range of applications. (3) By changing organic molecules, an enormous tuning of OIPs is possible.^{20, 21} Furthermore, they have advantages in flexibility, and low price of precursors. Interestingly, organic molecules can template inorganic octahedrons to make a different symmetry. Properties such as optical band gap and conductivity are also tuned.

To improve and change the morphology, scientists used a lot of organic cations, metal ions, and halides. Especially, D. B. Mitzi obtained many outstanding results in this field by synthesizing and characterizing large numbers of different OIPs. For example, the properties such as conductivity

were dependent on doping and substitution of metal ions. In the case of lead iodide-based OIPs, there are all Pb^{2+} ions in octahedron inorganic sites. The more we put Sn^{2+} instead of Pb^{2+} , (the higher doping level) the resistivity decreased from $10^7 \text{ } \Omega\text{cm}$ to $10^1 \text{ } \Omega\text{cm}$, and conductivity improved.²² Other metal ions whose valence is different from Pb can also be utilized as dopant in lead halide OIPs. Moreover, Mitzi also synthesized a metal-deficient distorted structure to generate more vacancies by not using +2 of divalent cations, but using +3 of trivalent cations doping such as Bi^{3+} and Sb^{3+} . $((\text{Org})\text{M}_{2/3}\text{I}_4, \text{Org} = \text{divalent cationic organic molecule}, \text{M} = \text{Bi}^{3+} \text{ and } \text{Sb}^{3+})$ ²³

Doping of organic molecules has also been studied to change properties of OIPs. For instance, by blending two different organic chains, people tuned resistivity. (Mixture of 1-butyl ammonium iodide and methyl ammonium iodide for tin-based iodide OIPs $(\text{C}_4\text{H}_9\text{NH}_3)_2(\text{CH}_3\text{NH}_3)_{n-1}\text{Sn}_n\text{I}_{3n+1}$)²⁴ As a result, when the ratio of methyl amine is getting higher, the structure was changed to a relatively conductive 3-dimensional structure. In the end, resistivity dramatically dropped from $10^6 \text{ } \Omega\text{cm}$ to $10^{-2} \text{ } \Omega\text{cm}$. In addition, by using a primary amine containing conjugated aromatic benzene ring, it was possible to synthesize electron-conductive 2-dimensional OIPs structure.²⁵ In the interlayer space surrounded by inorganic layers, aromatic rings were closed-packed, so that the electron pathway was formed to transport electrons in a certain direction. (Tin-based phenethyl amine OIPs, $(\text{C}_6\text{H}_5\text{C}_2\text{H}_4\text{NH}_3)_2\text{SnI}_4$) Through this directional pathway, the field-effect mobility was improved to $0.6 \text{ cm}^2/\text{V sec}$ in thin film transistor. Moreover, by using oligomer, $\text{H}_2\text{AEQT}(5,5''''\text{-bis-(aminoethyl)-2,2':5',2'':5'',2''''\text{-quarterthiophene})$ which

has conductivity and rigid diamine,²⁶ Mitzi synthesized electro-conductive OIPs that polythiophenes were in it. The structure of H₂AEQT OIPs was that primary amines in the end are plugged into the inorganic layer to make electrostatic bonding to make a stable structure. Through the rigid conductive organic oligomers, not only high conductivity, but also stable structure could be obtained by the confinement effect to make the inorganic layer get packed. These phenomena can also be applied in relatively unstable inorganic lattice to make a stabilized structure.

Halide ion doping also changed material properties of OIPs. In the case of 1-Butyl ammonium lead halide, (C₄H₉NH₃)₂PbX₄, halide ions from chloride to iodide changed the light absorbing maximum wavelength from 332 nm (UV region) to 504 nm. (Visible region) In other words, the optical band gap energy gets narrower from chloride to iodide.²⁷ In solar radiation, the portion of visible light is much larger than that of UV light. Therefore, visible light responsible iodide-involved OIPs are expected to be used as materials with high absorption efficiency and high photoluminescence effect. In figure 1.3, we summarized the previous works on OIPs tuning.

Application with various types of OIPs has been tried in the industry. A well-known application field was the thin-film transistor (TFT) and light emitting diode (LED).^{28, 29} A thin film of OIPs was fabricated on a gate oxide substrate by spin-coating. After that, metal electrodes were deposited onto OIPs. When we apply the voltage, OIPs-based LEDs generated light. Moreover, because OIPs show a characteristic absorption in the visible light region, they were applied in a photo luminescent device. OIPs can also be

functionalized in magnetic, dielectric, thermoelectric, and photoactive materials.³⁰

However, most of the previous researches only focus on the structural analysis and alkyl ammonium group. Including Mitzi, most did not try to change the plugging-in group in OIPs. If we make various types of organic molecules that can interact with the inorganic layer, it will be possible to attach an electron donating/withdrawing group, and electronegative functional groups for inductive effect. By utilizing electron density change caused by organic molecules, it will be possible to synthesize new OIPs with different properties. Following discussion is summarized in chapter 1.4.

1.1.2 Tolerance factor

To determine that synthesized OIPs have a 3-dimensional structure or a 2-dimensional structure, we should calculate the tolerance factor. For making closed packed perovskites lattice, (*Pm3m* space group) the size of organic chain should be exactly the same with the radius of the A site. In this case, organic cation is surrounded by 12 halide anions.

In 1926, Goldschmidt suggested the concept of tolerance factor (*t*) based on the relationship above.³¹ It is described as $t = (r_A + r_B) / \sqrt{2}(r_B + r_X)$. When *t* is equal to 1, synthesized perovskites can form a perfect crystal. At this time, the structure has exactly same as *Pm3m* space group. r_A , r_B , r_X indicate the ionic radius of A, B, X ions, respectively. In real system, *t* value

has the range for stable 3-dimensional cubic structure: from 0.78 to 1.05.³² (Not perfect cubic structure, but tetragonal structure with some distortion) If the t value is not in this range, only plugging-in group can be involved in the lattice, and dangling chains should be outside the inorganic layer which is a 2-dimensional perovskites. Although the tolerance factor is not available at high temperature and pressure, it is a powerful method to estimate the perovskite structure.

For example, when we think about the case of lead iodide, we can calculate the tolerance factor. Reported ionic radius of Pb^{2+} and I^- is 1.19 \AA ($= r_B$) and 2.20 \AA ($= r_X$), respectively. When t is equal to 0.78, the minimum radius of A is 2.55 \AA , and when t is equal to 1.05, the maximum radius is 3.84 \AA . Consequently, for fabricating 3-dimensional OIPs, the size of organic molecule in A site should be in a range of 2.55 \AA to 3.84 \AA . This value means that only two or three of C, N atoms of organic cation can be involved. Short organic chains can only make 3-dimensional perovskites structure, and if the organic chain is much longer, 2-dimensional OIPs should be formed.

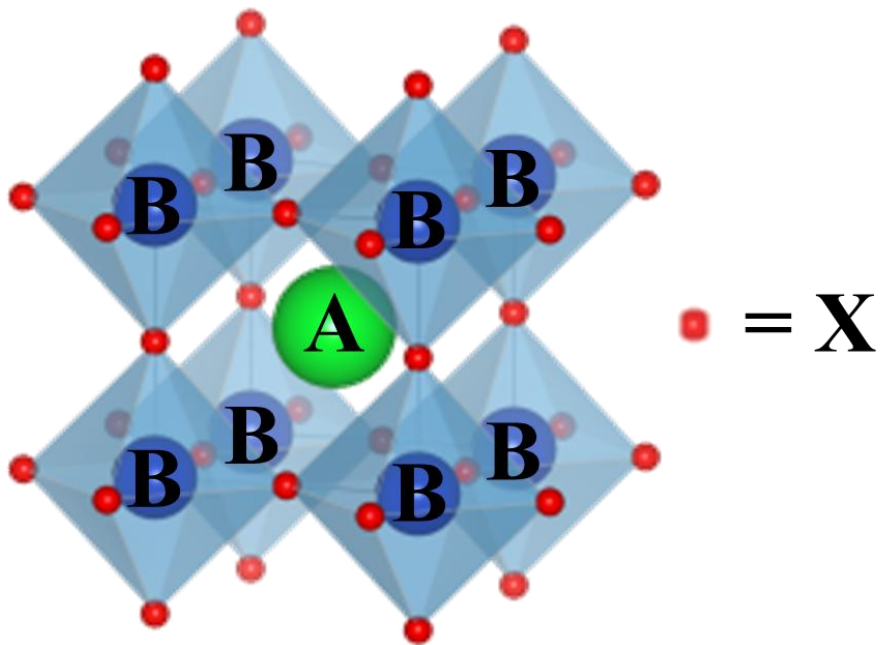


Figure 1.1 General crystal structure of metal halide perovskites. (ABX₃) In OIPs, bulky organic cations locate in the center of lattice (A site, (0,0,0)) with surrounding metal ions (B sites, (1/2,1/2,1/2)). Halide ions (X sites, (1/2,1/2,0)) locate at the center of plane.

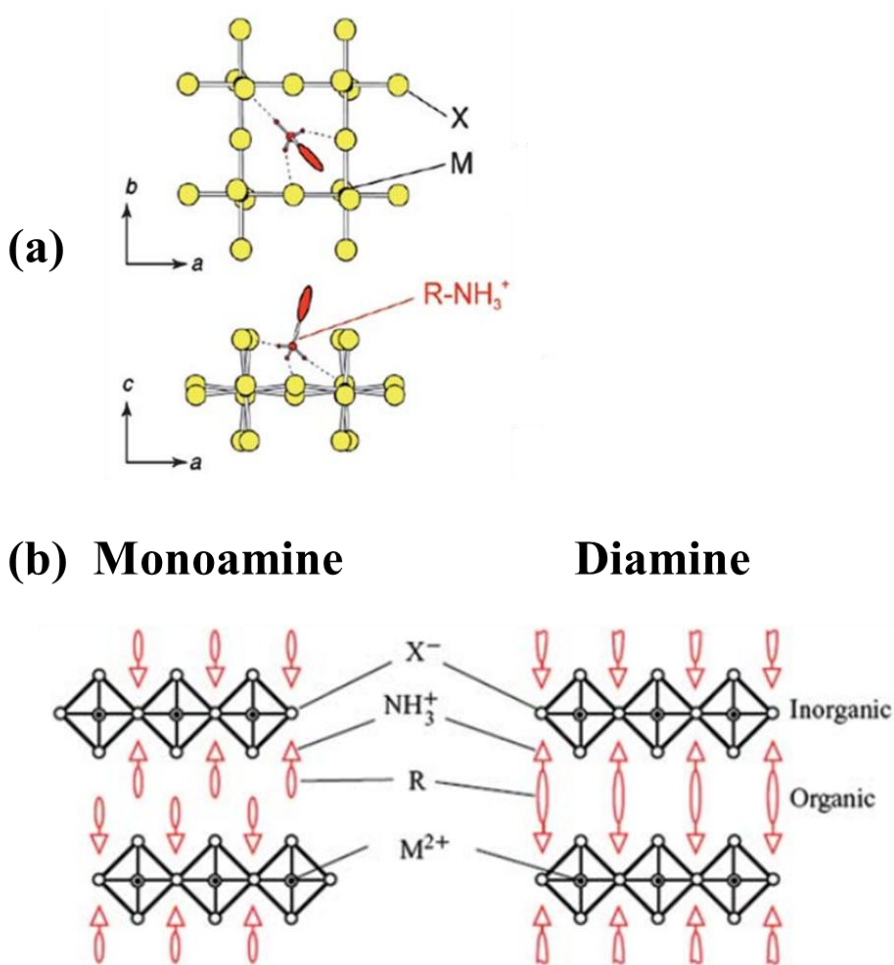


Figure 1.2 (a) Halogen bonding (dashed line) between plugged-in ammonium cation and inorganic layer. M and X indicate divalent metal ion and halide ion, respectively. (b) Structural difference depending on the number of amine in organic alkyl chain. Arrows indicate ammonium ion, and R groups indicate extended alkyl chain. Diamine molecules can bind both upper and lower inorganic layers.

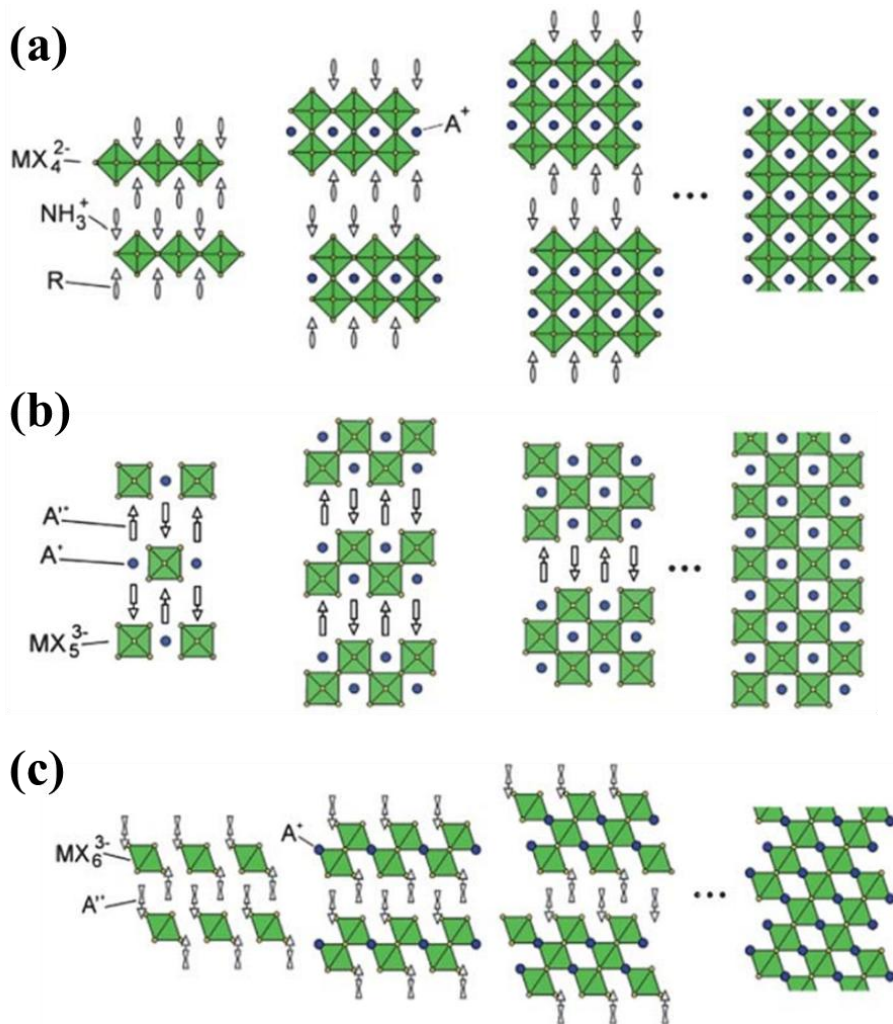


Figure 1.3 Different structures of 2-dimensional OIPs. (a) $\langle 100 \rangle$ -oriented, (b) $\langle 110 \rangle$ -oriented, and (c) $\langle 111 \rangle$ -oriented structure. (a) is the most thermodynamically stable structure among these three structures.

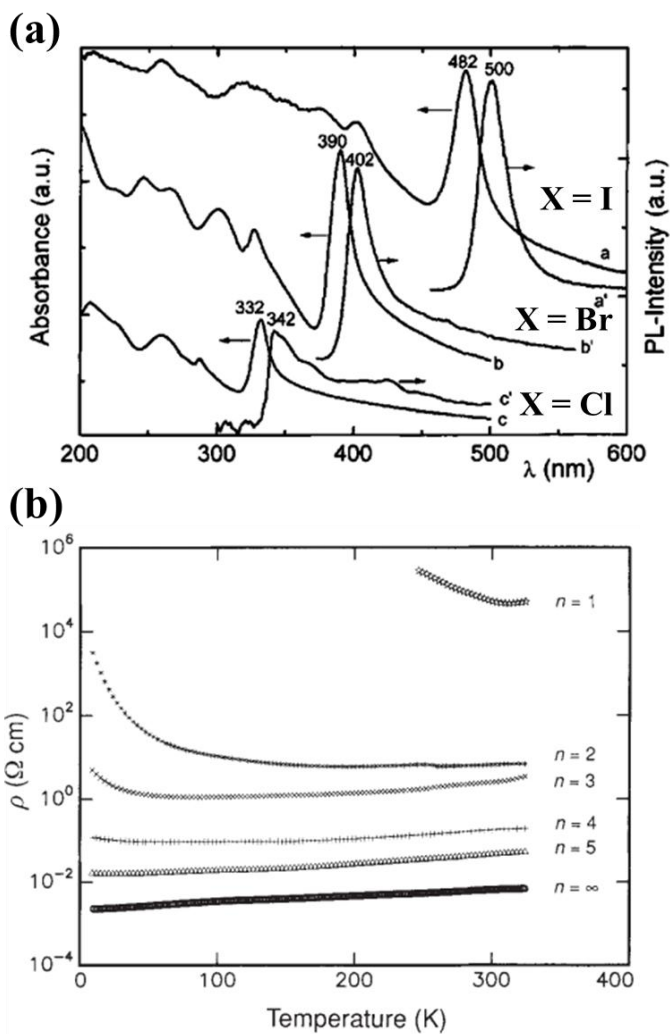


Figure 1.4 (a) Halide ion dependence of $(C_5H_4CH_2NH_3)_2PbX_4$ OIPs Iodide ion has narrow band gap energy compared to other halide ions. (b) Organic chain dependence of $(C_4H_9NH_3)_2(CH_3NH_3)_{n-1}Sn_nI_{3n+1}$ OIPs. When the value of n increased, the resistivity starts to be lowered. It means that 3-dimensional OIPs structure is more conductive.

1.2 Solid-state perovskite solar cells

Dye-sensitized solar cell (DSSCs) is a type of thin film solar cell and was first developed by Brian O' Regan and Michael Gratzel, hence also called as Gratzel cell.³³ Among the many advantages of DSSCs, simple fabrication process and low fabrication costs compared with the silicon based conventional cells are considered as the main advantage of DSSCs. Also, it has a relatively high solar-to-electrical energy conversion efficiency considering its structure is thin-film based. Furthermore, being able to work in a low density of light makes it possible to operate in non-direct sunlight and bad weather conditions. Being able to cool down easily from high temperature makes DSSCs operate in a relatively high temperature with low operating temperatures. In addition to this, it is light weight and can be used in a small area, especially on the outer surface of a building with decorating functionalities as a various color dyes can be used.³⁴

Due to these advantages, DSSCs received significant attention in the field as an environmentally friendly technology with being able to produce electricity from the decorating glass wall used on building walls or being able to be practically used as an outdoor solar cell. Furthermore, DSSCs are used in automobiles or motorcycles instead of silicon cells which can be fragile.

However, there are two main disadvantages of ordinary DSSCs and one of them is related to electrolyte. In DSSCs, liquid electrolyte is normally used, which makes DSSCs difficult to adjust itself to temperature change. For example, rise in temperature can cause evaporation of inner electrolyte or

even breakdown of the whole structure. The evaporated volatile electrolyte liquid can even cause harm to a human body or surrounding environments. However, in the case of decrease in temperature, the electrolyte liquid may freeze, causing a cut-off in power generation. Thus, this issue of temperature stability of electrolyte may cause a long term stability issue in DSSCs.³⁵

In addition to this, the other major issue of DSSCs may lie in using photosensitizer as ruthenium dye or platinum catalyst.³⁶ These noble metal compounds can be very expensive and may bring down the life expectancy of the device due to rapid decrease in device efficiency caused by poisoning of the compounds when they are exposed to a strong ligand such as carbon monoxide. Moreover, liquid electrolyte can also cause desorption and degradation of dye.

In order to overcome these problems, many studies on changing electrolyte into quasi-solid form using solids or organic materials such as p-type semiconductor are still in progress. In 1995, the Tennakone research group has first proposed all-solid state DSSCs using TiO_2 as a n-type semiconductor and CuI as a p-type semiconductor, and the photocurrent was generated by injection of an electron-hole pair produced from dye into each semiconductor.³⁷ Since then the device efficiency in the early stage, which was 0.8%, has continuously increased by using organic materials such as CuSCN or spiro-MeOTAD as a p-type material.³⁸

The main advantage of solid-state DSSCs is that it is operationally more stable compared to the previous DSSCs. Also, compared to liquid photovoltaic cells there is no leakage and corrosion. Moreover, due to easiness

in generation and transportation of separated charges compared to the conventional cell, material qualities including purity and crystallinity is not as critical as that of the conventional photovoltaic cells.³⁹

1.2.1 Structure and mechanism

For scientific understanding, we should focus on the structure of the solid-state cells. The cell structure can be separated into three big parts. (Figure 1.5) At the anode part, n-type semiconductor TiO_2 is deposited onto transparent conducting oxide. Furthermore, on that layer, p-type semiconductor or hole transfer materials are deposited. Hole transfer material makes contact with the metal electrode, to generate one total circuit. Generally, previous studies made TiO_2 a mesoporous structure to load more sensitizer by filling small pores in it.⁴⁰

For operating solar cells, an electron-hole pair should be formed, induced by light exposure in the photosensitizer. This pair is the so-called exciton. The formed light-induced electrons are injected into photoanode TiO_2 , otherwise generated holes are going to hole transfer materials. In order to operate this system, the LUMO (Lowest Unoccupied Molecular Orbital) state of dye should be located higher than the conduction band edge of TiO_2 , while the HOMO (Highest Occupied Molecular Orbital) state of dye should be located lower than the redox potential of the hole transfer material.

Now, let's focus on each component in detail. For photoanode, there are

several conditions in which fast electron transporting ability and proper energy level takes generated electron from dye molecules without loss. In addition, good adhesion to the electrode semiconductor and large surface area to absorb more dye are needed. Until now, research related to matching the band alignment was studied by using SnO₂, whose conduction band is about 0.5 eV lower than that of TiO₂, or ZnO whose electron mobility is high enough to improve the electron injection kinetics instead of TiO₂.⁴¹ Nanostructures (nanoparticles, nanorods, core-shell structures) of TiO₂ were also performed to enlarge the surface area for high efficiency solar cells.^{42, 43}

In the case of the sensitizer, it should have a panchromatic property that is a photoactive property to generate exciton by exposure to light. To be a high efficient photosensitizer, it should be not only be thermally/chemically stable, but also chemically well-bonded on the photoanode without desorption, and have a low recombination rate. Metal complex is a well-known sensitizer.^{44, 45} Noble metals including ruthenium, osmium, and platinum bonded with organic ligands show a long lifetime of exciton, and extensive light absorption under visible light. However, they are expensive and difficult to purify, so people developed organic dyes such as cumarins, indolines, porphyrins, squarines.^{46, 47} Nowadays, organic-inorganic perovskites are utilized as a sensitizer to maximize the efficiency. It will be discussed in 1.2.2 in detail.

Finally, the hole transfer materials are the key materials in solid-state cells. These materials conduct holes generated from the sensitizer, so that these should be p-type, and conductive. In addition, because the recombination rate in the sensitizer is generally slower than the regeneration rate in hole transfer

materials, they should recover quickly to overcome diffusion-limited kinetics.⁴⁸ In the past, copper-based solid materials (CuI, CuSCN) were utilized, but they were highly toxic, thus not environmental friendly. Therefore, they are replaced by organic molecules. Polymer candidates which have hole injection properties are PTAA, PCDTBT, PCPDTBT, P3HT.^{49, 50} Recently, spiro-MeOTAD, the molecular hole transfer material, attracts a lot of interest to improve contact with dye and interface properties.⁵¹

To evaluate solar cells' properties, there are four parameters; J_{SC} , V_{OC} , fill factor, and efficiency. By analyzing the I-V curve, it is possible to calculate them. J_{SC} is the current density when the external voltage is zero. This current density is equal to the total current generated by the photons. Otherwise, V_{OC} is the voltage when the current density is zero. Ideally, this voltage is the same to the potential gap between n-type materials and p-type materials. Fill factor is the factor that determines the efficiency. The fill factor can be calculated by the maximum area of a rectangle on the I-V curve. In other words, it is the ratio between the product of J_{SC} , V_{OC} and the product of J and V where cell has the maximum power. Efficiency (η) is determined by the above three parameters, and is expressed as $\eta = (J_{SC})(V_{OC})(\text{Fill factor})$. The efficiency is also known as the power conversion efficiency. The four parameters are related with certain phenomena in solar cells, so an exact understanding of four parameters is needed to improve them.⁵²

To get high cell properties, we should generate high J_{SC} , V_{OC} and fill factor. To increase J_{SC} , the diffusion of separated electron-hole pair to electrode should be fast. The larger the diffusion coefficient, the higher J_{SC} they have.

For this, adding alkaline ions or improving dye absorption on TiO_2 have been attempted to get high J_{SC} . V_{OC} is affected by exciton lifetime. The band difference between phoanode and hole transfer materials determines V_{OC} , so that the lifetime of exciton has been studied to generate high voltage from the cell. The case of the fill factor is a little bit more complicated. The fill factor is affected by two parameters; series resistance (R_s) and shunt resistance (R_{sh}). R_s is the slope in the I-V curve along the x-axis which means the internal cell resistivity. It means that there is a high energy loss if there is a high R_s , so that R_s should be decreased for high efficiency. Methods including interface control to improve the contact between electrode and semiconductor have been studied. On the other hand, R_{sh} means the slope along the y-axis in the I-V curve, related with the recombination of the electron-hole pair. High R_{sh} has a high fill factor: to decrease defect sites for reducing recombination, or leakage current can increase the R_{sh} value.⁵³ (Figure 1.6) In this paper, the following analysis and discussions were based on the four parameters.

Until now, we have focused on solid-state solar cells from a different point of view. However, there are limits in the cell. For example, ordinary solid electrolyte only generate smaller amounts of power than liquid electrolyte, and the poor interfacial contact between porous TiO_2 layer and hole transfer materials which makes a barrier to conduct the electron-hole pair from sensitizer to electrode. Additionally, low conductivity of solid materials also lowers the cell efficiency.

To improve the problems of solids-state DSSCs, people have tried to approach them with two methods. One method is changing the dye into other

materials. Unlike ordinary dyes, the new dye should be stable under oxidative atmospheres and have low price of metal complex using cheap metal ion. When we improve the photosensitizing effect dramatically, commercial fabrication of DSSCs will be possible.

The second method is the improvement of contact between p-type hole transfer materials and the n-type TiO₂ layer. In the past, electrochemical deposition was performed to make a fine interface. For example, Gratzel successfully deposited ZnO and CuSCN on the solid-state cell to make a complete form of solid cell.⁵⁴ However, this method had side effects which included dye decomposition, making it unsuitable for long term applications. Instead of electrochemical deposition, there is the solution method. Fabrication of solution-based DSSCs makes better penetration of solution into porous TiO₂ film perfectly, so that it makes high hole injection property. In addition, the solution-based method is easy and simple to coat for fabricating the solar cell in a fast, economical way.

1.2.2 Current research on perovskites photosensitizer

Previous solid-state DSSCs have only a few percent of efficiency. This value is lower than the conventional silicon cell, whose efficiency is 15% (Figure 1.8) As a result, the development of new sensitizer is essential to improve the cell efficiency.

In 2012, both N. G. Park's research group⁵⁵ and H. Snaith's group⁵⁶

successfully fabricated solid-state solar cells with an efficiency of 10% by using organic-inorganic perovskites hybrid materials as photosensitizers. (Figure 1.7) This breakthrough came from the light absorbing behavior of methyl ammonium lead iodide, or MPI perovskites.

MPI can be synthesized by the reaction between organic iodide salt and lead iodide. The salt came from methyl amine and hydriodic acid combined with inorganic lead iodide to form 3D perovskites. The dark grey colored MPI has several advantages: easy synthesis, high charge mobility, solution-based process with improved interface, and high absorption coefficient with visible light. For these reasons, the thin film cell fabrication is possible by high contact with n-type TiO_2 and MPI. If we look at the band structure, valence band is located at -5.43 eV, and the conduction band is located at -3.93 eV.^{57,58} The band structure shows that the electron can be injected from the higher MPI conduction band into the lower conduction band in TiO_2 semiconductors, whose position is about -4.0 eV.

The reason of the outstanding photo-responsible properties of MPI is now in dispute. One suggestion from Gratzel is that MPI perovskites act as an effective photosensitizer by easily making light-induced exciton and easily injecting them into semiconductors.⁵⁹ The other suggestion from Snaith is that cell performance stems from unique material properties of MPI. In fact, MPI is a bipolar semiconductor, so it has both p/n-type in the structure to make the solid cell a junction cell.⁶⁰

Until now, MPI perovskites sensitizer has been utilized as brand-new materials for solid-state solar cells. Through MPI, many researches are

performed with various methods. In 2009, the first trial of application of MPI perovskites as sensitizer in liquid cell was developed by T. Miyasaka's group.⁶¹ S. I. Seok's group reported that various hole conducting materials including PTAA, P3HT had an advantage in improving MPI cell properties.⁶² In addition, D. Angelis' group analyzed the structure and property of MPI with a materials-scientific approach by halogen doping or tin doping.⁶³ A. Hagfeldt's group tried to use different types of n-type semiconductors such as ZrO_2 and ZnO instead of TiO_2 .⁶⁴ Through these numerous approaches, the efficiency of MPI-based solid-state perovskite cells has been recorded to be approximately 16%.

Although perovskite sensitizers attract a lot of interests instead of ordinary dye, MPI solid-state solar cells also have their limits. In chapter 1.4, we will deal with the disadvantages of MPI, and suggest the direction to overcome the limits of perovskites solid cells.

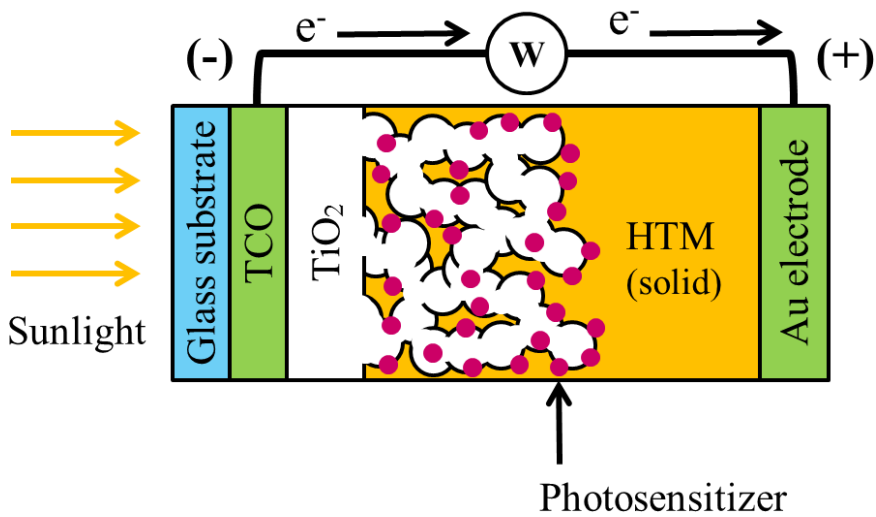


Figure 1.5 Schematic structure of solid-state solar cells. TCO indicates transparent conducting oxide, and HTM indicates that hole transfer material. When the sensitizer absorbs the light, it goes to excited state. Excited sensitizer injects electrons into TiO₂ conduction band, and also injects holes into HTM at the same time. Separated electrons and holes make the flow of electrons: this is what we observed from solar cells.

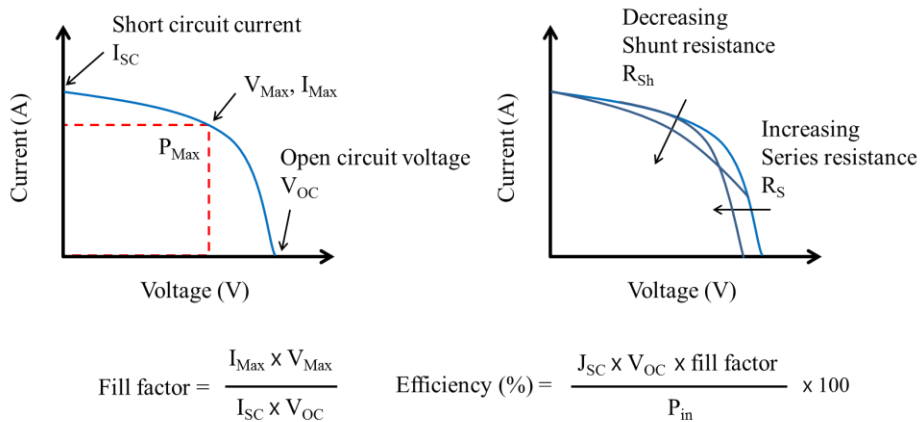
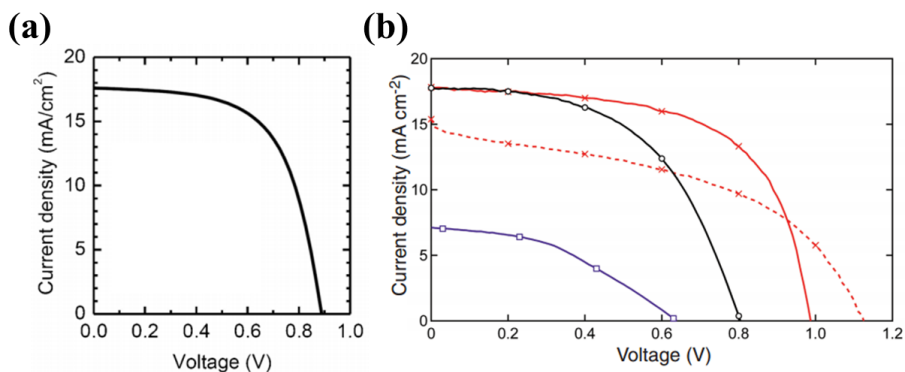


Figure 1.6 I-V curve analysis to get J_{sc} , V_{oc} , fill factor, and efficiency. J_{sc} is current density, and I_{sc} per unit area. P_{Max} is the point that generates maximum power: the product of current and voltage. To get the high efficiency, high J_{sc} , V_{oc} and fill factor value are needed. For maximizing the fill factor, R_{sh} should be increased, otherwise R_s should be decreased.



	Result (a)	Result (b)
J_{SC}	17.6 mA/cm ²	17.8 mA/cm ²
V_{OC}	0.89 V	0.98 V
Fill factor	0.62	0.63
Efficiency	9.7 %	10.9 %

Figure 1.7 The first report of OIPs-based solid-state solar cells. Both results were published in 2012. The breakthrough of cell efficiency was achieved by $(CH_3NH_3)PbI_3$ (MPI) which is one of OIPs. Nowadays, the maximum efficiency of MPI cell is about 16%. (a) is from N. G. Park's group, and (b) is from H. Snaith's group. The cell parameters are summarized in the table below.

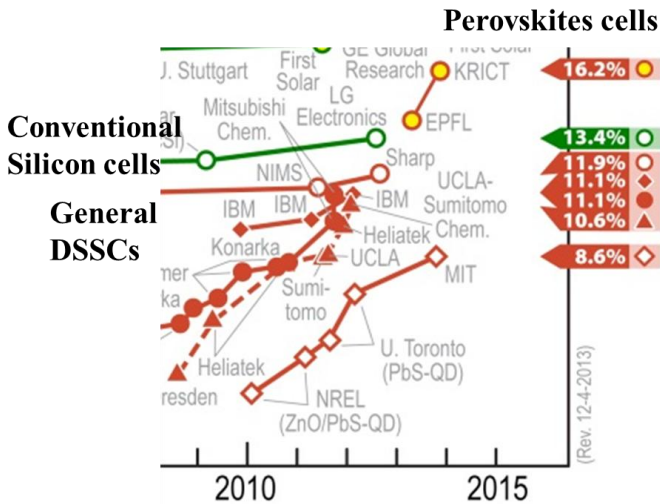
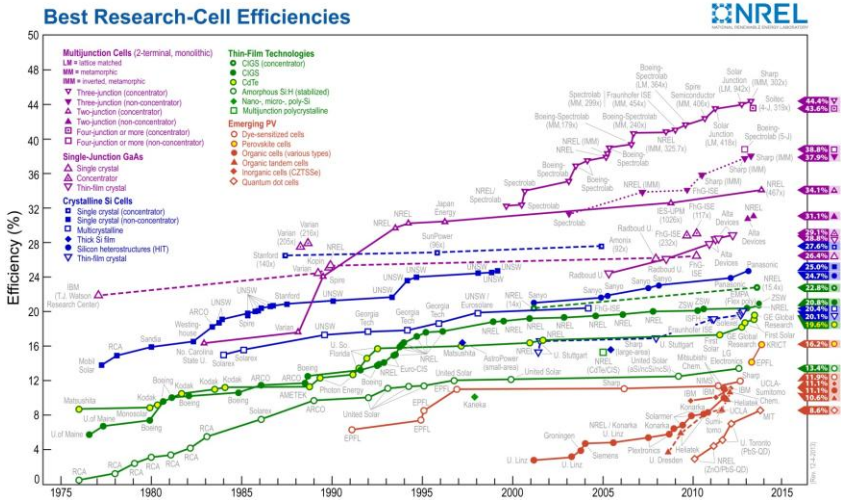


Figure 1.8 World-recording cell efficiencies in solar cell industry. It is worth noting that perovskites cells generate higher efficiency than DSSCs and conventional amorphous silicon cells. (National Center for Photovoltaics, NREL, United States)⁶⁵

1.3 Imidazole-based materials

Nitrogen-containing aromatic molecules including pyridine, imidazole, and pyrrole are in one kind of hetero-atom ring group. Unlike the 6-membered ring of pyridine, imidazole and pyrrole has a 5-membered ring which contains two and one nitrogen atom, respectively. (Figure 1.9)

Interestingly, planar imidazole groups are in the biological system as a significant building block. The ring can be found in a lot of biomolecules including histidine ($C_6H_9N_3O_2$), which is one of the essential amino acids, and histamine, ($C_5H_9N_3$) which is well-known hormone in the local immune responses. In nature, histidine and histamine mainly play the role as binding factors or catalytic sites by interacting with metal ions. Especially, histidine exhibits outstanding metal binding properties with nickel, copper, zinc, and cadmium.^{66, 67} Many researchers have reported that nitrogen atoms in histidine ring helps make electrostatic bonding. Through the characteristic binding affinity of the imidazole ring, it is now used as an interconnecting bridge for synthetic materials. For example, heavy metal detecting sensor with histidine-tagged molecules by metal binding, or intercalation reagents penetrated in a semiconductor.

Nowadays, imidazole containing molecules attract a lot of attention in the field of metal-organic framework.⁶⁸ (MOFs) Imidazole derivatives as MOFs donor has a strong tendency to make a helical structure which shows chirality along the axial direction.⁶⁹ Plus, the imidazole ring can be functionalized easily. Through these advantages, scientists have tried to fabricate various

types of MOFs structures. Xu's group synthesized a multifunctional imidazole ring attached to a positively charged MOFs acceptor.⁷⁰ As a result, the helical structure was transferred to whole MOFs networks by interconnection. On the other hand, highly flexible MOFs could be formed by functionalization with long alkyl chains. Additionally, due to the planar structure and metal binding affinity of the imidazole, Zhao's group fabricated the 2D structured MOFs.⁷¹ A functionalized imidazole with aryl group or protons make planar morphology with copper or metal chalcogenide.⁷² Without any complexity, this lamellar MOFs structure is comparable to previous 3D structures. In 2002, the new paradigm of MOFs structure known as ZIFs (zeolitic imidazole frameworks) was also reported.⁷³

As we can notice through the research trend, imidazole-involved materials are now investigated a lot as binding factor with metal ion or semiconductors. Imidazole could be utilized in a wide range of materials not only by convergence point with biomolecules, but also by outstanding binding affinity and structural benefits,

1.4 Research scope and design

1.4.1 The bottleneck of $(\text{CH}_3\text{NH}_3)\text{PbI}_3$ photosensitizer

Methyl ammonium lead iodide $(\text{CH}_3\text{NH}_3)\text{PbI}_3$, or MPI is 3-dimensional organic-inorganic perovskite which is now a cutting-edge material for

photosensitizer in solid-state solar cells.⁷⁴ ($E_g = 1.5$ eV) MPI has a low exciton binding energy (~ 45 meV) which means that the lifetime of the photo-generated electron-hole pair is long enough to be survived.⁷⁵ However, there are two major disadvantages of MPI. In this chapter, we focused on the bottleneck of MPI, and then we suggested a new approach with imidazole ring-involved OIPs for solid-state photosensitizer.

First of all, the most serious problem of MPI is stability. As we mentioned in chapter 1.1, methyl ammonium cation takes the center position, surrounded by PbI_4 inorganic layers. The electrostatic interaction among methyl ammonium cations and lead or iodide ions is the key binding factor for stabilizing the perovskites structure. However, when we exposed MPI in highly humid atmospheres, the water molecules started to get into the A site of perovskites instead of methyl ammonium ions. The reason is that the interaction parameter related with molecular polarity and solubility is much stronger in water and lead iodide than in organic cation and lead iodide. As a result, the MPI structure started to decompose to make a PbI_2 precursor and methyl ammonium aqueous solution. Low water-resistance makes MPI difficult to use in the commercial market. Stability of MPI should be guaranteed under heating, humidity, and UV light.

Second, tuning of MPI is hard to deal with. Many research groups have tried to change the band gap or absorption coefficient through various tuning methods including doping or substitution. However, they only focused on the metal or halide ions: organic chain dependence was confirmed by few researches. For this reason, there is a small potential to change the structure.

For example, if we substitute Pb to Sn, the conductivity value can be increased, and band gap energy can be decreased from 1.5 eV to 1.24 eV. However, tin-doped MPI does not act as an effective photosensitizer because of the high conductivity.⁷⁶ On the other hand, if we substitute iodide to bromide, the band gap energy can be increased from 1.5 eV to 2.0 eV.⁷⁷ Although chlorine or bromine-doped MPI shows improved charge transporting performance in a ratio of 1 (bromide dopant) : 3 (iodide), the band gap energy gets too large to absorb visible light.⁷⁸ For this reason, the color of methyl ammonium lead bromide is red ~ orange, and that of methyl ammonium lead chloride is almost white without any visible light interaction.

Until now, only few researches about organic molecule doping in OIPs have been reported. Instead of methyl ammonium salt, N. G. Park's group developed ethyl ammonium-based lead iodide, $(\text{CH}_3\text{CH}_2\text{NH}_3)\text{PbI}_3$, whose band gap was 2.2 eV, and the efficiency in liquid cell was 2.4 %.⁷⁹ On the other hand, Mhaisalkar's group suggested new 3-dimensional OIPs containing formamidinium $\text{HC}(\text{NH}_2)_2^+$ molecules.⁸⁰ However, their researches also have limits. They only handled 3-dimensional OIPs without concerning other structures.

Unfortunately, previously reported various types of OIPs were only utilized in crystal analysis, thin-film transistor, LED, and photoluminescent materials. Although their structures were well-defined, optical properties such as band structure was not confirmed yet. In other words, only few OIPs have been applied as energy materials for exciton generation. It is necessary to search other OIPs candidates which have photosensitizing activity for overcoming

the innate bottleneck of MPI.

1.4.2 Advantages of imidazole-based OIPs photosensitizer

In order to overcome the bottleneck of MPI, a different approach is needed. Halide doping or metal doping is almost done, and there are only a few vacancies to get more useful information. Therefore, in this paper, we concentrated on the topic with organic molecule doping in lead iodide system by using new-organic molecules: imidazoles.

Firstly, derivatives of imidazole ring have cationic (+) charge in acidic condition. It means these molecules can make electrostatic interaction with inorganic parts in OIPs. Secondly, the size of imidazole ring is 3.1 Å which is in the range of tolerance factor for Pb-I system. (2.55 Å ~ 3.84 Å) For these reasons, we designed imidazole ring as plugging-in group for new OIPs.

If we can synthesize imidazole-based OIPs, there would be four major advantages: (1) Water stability should be increased. In the case of methyl amine, there is one primary amine for making a bond with lead iodide. On the other hand, imidazole has at least two binding sites. In addition, imidazole makes more efficient bonds because it is a secondary amine: the basicity of primary amine is stronger than secondary amine, which makes imidazole donate fewer electrons to hydrogens to make them more positively charged.⁸¹ Consequently, increased binding sites and hydrogen binding affinity by electron sharing lets imidazole-involved OIPs to be relatively stable in humid

atmospheres compared to MPI. In other words, it is difficult for water molecules to disturb the imidazole perovskites structure.

(2) It is possible to suggest a new plugging-in group of OIPs. In previous studies, primary amine at alkyl chain made electrostatic interaction with inorganic layers. If the whole imidazole ring bonds with metal halides, it will be a new paradigm that not only primary amine, but also other organic chains can be involved in as plugging-in groups. We can show a lot of potential in organic molecular variation.

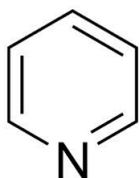
(3) Even imidazole-containing biomolecules can form OIPs with metal halide. It is worth noting that there are many biomaterials that have an imidazole ring. Bio-hybridized materials are now considerably important, such as sea-shells, which is the composite of calcium carbonate and biopolymer matrix. If we use them, we can construct new hybrid materials with bio-system: peptide-bonded inorganic semiconductor which shows a collaborative property. In addition, most biomolecules have chirality. Therefore, we can fabricate chirality-induced inorganic materials, or light-active materials depending on polarized light source.

(4) Tuning of lead iodide by organic molecular change is possible. Compared to recent MPI researches, we can suggest tuning of color or band gap energy with various molecular cations. It means that there is now a potential to change more variables by organic side chains, and more chances to make fine-tunable photosensitizing OIPs to get appropriate band structure for solid-state cells. Dependence of metal halide perovskites on organic molecules can be a new topic for researchers in this field.

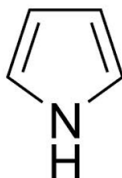
In this research, we used two basic imidazole-based molecules: histidine ($C_6H_9N_3O_2$) and histamine ($C_5H_9N_3$). Their molecular structure and molecular weight are summarized in figure 1.9. Through the synthetic methods in previous PbI_2 -based OIPs researches, we succeeded in synthesizing the histidine lead iodide (HPI), and histidine lead iodide (hPI) in a similar way. There are two reasons why we chose the PbI_2 semiconductor. One is that iodide salt has outstanding optoelectronic properties and a suitable band gap for absorbing visible lights as a photosensitizer that can drive high cell performance. The other is that lead-based perovskites have appropriate exciton binding energy compared to tin, and of course, the size of the lead cation is well-matched with bulky organic molecules. Our experimental methods are introduced in the following chapters.

(a) N-involved aromatic rings

Pyridine



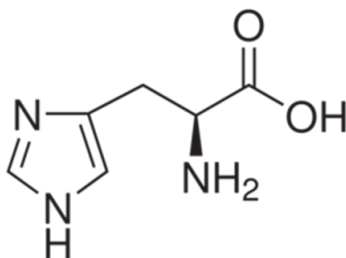
Pyrrole



Imidazole



(b) Histidine ($C_6H_9N_3O_2$)
(M.W. = 155.15)



Histamine ($C_5H_9N_3$)
(M.W. = 111.15)

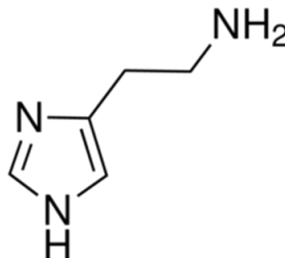


Figure 1.9 (a) Different types of nitrogen-involved hetero-atom aromatic rings. Imidazole has 5-membered ring with two of secondary amines. (b) Chemical structure and molecular weight of histidine and histamine.

Chapter 2. Experimental and Procedure

2.1 Imidazole-based organic-inorganic perovskites

2.1.1 Materials

Lead iodide (PbI_2 , 99%) was purchased from Sigma-Aldrich company, and hydriodic acid (HI, unstabilized 57% aqueous solution), L-histidine ($\text{C}_6\text{H}_9\text{N}_3\text{O}_2$, 98%), histamine ($\text{C}_5\text{H}_9\text{N}_3$, 97%) were purchased from ACROS company. In addition, methyl amine (CH_3NH_2 , 40% in ethanol, TCI) was purchased for MPI as reference material. Organic solvents including diethyl ether ($\text{C}_4\text{H}_{10}\text{O}$, 99% for HPLC), γ -butyrolactone ($\text{C}_4\text{H}_6\text{O}_2$, 99%), N,N-dimethylformamide (DMF) ($\text{C}_3\text{H}_7\text{NO}$, 99.5%), and dimethyl sulfoxide (DMSO) ($\text{C}_2\text{H}_6\text{SO}$, 99.5%) were purchased from DAEJUNG chemicals. We used two substrates; one was that p-type silicon wafer which has 10-15 Ω resistivity (Silicon Materials Inc., 525 μm) and the other was fluorine-doped tin oxide (FTO) substrate which had 15 Ω /square surface resistivity. (TEC-8, precut as 1.0 cm by 1.5 cm from Pilkington Company)

2.1.2 Synthesis of imidazolium iodide precursors

The histidine iodide and histamine iodide salt were prepared based on the

acid-base chemistry. Imidazole ring and primary amine group in histidine or histamine can react with strong acid such as HI. ($pK_a < 1$)⁸² As a result, they formed organic cation iodide salt. Both histidine and histamine contain two reaction sites (imidazole ring and primary amine) which can be combined with iodide anion, to generate beige color of dication-protonated ammonium salt.

The reaction between organic precursor and HI was the prime factor in order to synthesize the salt in detail. We mixed 5 mmol of histidine (or histamine) into 50 mL of distilled water. When the homogeneous solution is formed, 6 mmol of HI (1.16 mL) was slowly added to the mixture with magnetic stirring. The reaction was conducted at 0°C with ice cooling for 2 hours. Unlike imidazole-based organic molecules, white color of methyl ammonium iodide was synthesized directly by the reaction between methyl amine solution and HI without additional water.

After the first step, the solution was dried using rotary evaporator. To achieve high quality of salt, temperature should remain under 50°C for one hour. When the solvent has been fully evaporated, we washed the synthesized salt using diethyl ether several times until the color of salt turned to mild beige. Remaining HI was entirely removed during this process. When the washing was completed, the salt was moved into vacuum furnace was stored for 12 hours. At 70°C, the synthesized salt was completely dried and prepared to use. (Figure 2.1)

2.1.3 Synthesis of imidazole-based OIPs

To synthesize organic-inorganic perovskites solution, we used two different organic solvents: γ -butyrolactone and DMF. Primarily, 1 mL of DMF or γ -butyrolactone solvent was heated in the vial at 60°C. Proceeding that, we added PbI₂ powder into the heated solvent. In contrast to its usually high solubility of PbI₂ in DMF, it was not soluble in γ -butyrolactone. To maintain the homogeneous reaction, magnetic stirring was needed. When the temperature of mixture maintained 60°C, we added equimolar of synthesized imidazolium iodide salts into the mixture, and observed it overnight. Depending on the concentration, the amounts of PbI₂ and salts were differentiated.

2.1.4 Single crystal preparation

The histidine lead iodide (HPI) single crystal was prepared by vapor diffusion method. This method required two different types of organic solvents; one was highly HPI soluble solvent (DMF), and the other was volatile insoluble solvent. (Acetonitrile) In closed system, the HPI-saturated DMF solution has lower vapor pressure than acetonitrile. Consequently, vaporized acetonitrile molecules were diffused into DMF solution decreasing the solubility of HPI. (Figure 2.2, (c)) In the oversaturated HPI-DMF solution, the crystal started to nuclearize and to grow to make the single crystal. The

speed of diffusion rate could be controlled by the temperature. The vapor diffusion is an expedient/effective/efficient method when there is a minute number of crystal seeds.⁸³

On the other hand, the histamine lead iodide (hPI) single crystal was prepared with a different methodology. It is because hPI insoluble organic solvent was hard to find out. Therefore, we used the slow-cooling method to acquire a single crystal of hPI. (Figure 2.2, (b)) We mixed 1 mmol of PbI_2 and 1 mmol of HI in 10 mL of distilled water. After then, this mixture was refluxed and heated to 90°C for 3 hours. This synthesized brown-colored solution was then moved into the heat block container for slow cooling from 90°C to room temperature. When cooling was completed, shiny oblong single crystal of hPI was obtained.

2.2 Solar cells fabrication

2.2.1 Fabrication methods

For the solid-state DSSCs with OIPs sensitizer, we used FTO glass as a substrate. The conduction of sol-gel process fabricated a compact layer of anatase TiO_2 (c- TiO_2) Titanium isopropoxide ($\text{Ti}(\text{OCH}(\text{CH}_3)_2)_4$, 97%, Sigma-Aldrich) in co-solvent of ethanol and distilled water was mixed with nitric acid for hydrolysis and the mole ratio of Ti-source : water : nitric acid was 1:4:0.04.⁸⁴ At room temperature, spin-coating was taken at 3000 rpm 30 sec to

make 50 nm thickness of c-TiO₂ layer. After the coating, substrates were baked at 150°C for 5 min. To form the blocking layer, TiCl₄ was additionally coated with 40mM of aqueous solution at 70°C 30 min. When the coating of c-TiO₂ was finished, we annealed the films at 500°C for 30 min.

Above the c-TiO₂ layer, mesoporous TiO₂ should be coated as a photosensitizer absorber. Dyesol TiO₂ paste (20 nm of TiO₂ anatase particles) was diluted in ethanol and spin-coated at 2000 rpm 20 sec. After the coating, TiO₂ substrates were annealed at 500°C for 1 hour. Fabricated mp-film through this process had 500~600nm of thickness.

Finally, OIPs solution was deposited on fabricated c-TiO₂/mp-TiO₂ substrates. The rpm of spin-coating was 4000 rpm and the coating time was 30 sec after 20 sec of holding. Baking process was treated on OIPs coating at 100°C for 45 min. After the baking, hole transfer materials, spiro-MeOTAD (C₈₁H₆₈N₄O₈, Merck) was coated with the mixture of chlorobenzene, acetonitrile, LiTFSI (Lithium bis(trifluoromethanes) sulfoimide), and tert-butyl pyridine. Without annealing, spiro-MeOTAD started to dry up to make the contact with OIPs coating. For the final step of DSSCs fabrication, four gold electrodes were deposited on the cell with the thermal evaporator (ULTECH).

All materials were purchased from Sigma-Aldrich without any purification. To avoid the negative effects caused by the moisture or oxygen, we fabricated whole steps in N₂ glove box. Summarized methods are in figure 2.3.

2.2.2 Coating techniques of OIPs photosensitizer

For the high-efficient DSSCs, the interface control is extremely significant. Subsequently, the coating techniques should be investigated to get the well-controlled interface. Recently, there are two coating methods for OIPs coating: spin-coating and dip-coating.

2.2.2.1 One-step spin-coating

For high quality spin-coating, the homogeneous OIPs solution should be prepared. If there are any impurities in solution, the coating cannot produce uniform result. Therefore, we used 60°C maintained OIPs solution to eliminate impure solutes and reactants. With this solution, OIPs were coated on FTO substrate with 2000 rpm 40 sec. (ACE-200 spin coater, Basic condition)

To improve the interface, we treated two different methods: plasma treatment and preheating. The plasma treatment (SNTEK) of FTO glass was carried out with a 100 W radio-frequency power for 10 min under 140 mTorr. On the other hand, the preheating was carried out at 100°C until the substrate reaches to the temperature equilibrium. The dependence of solvent, plasma treatment, and preheating will be introduced in chapter 3.2.

2.2.2.2 Two-step dip-coating

Compared to spin-coating, dip-coating needed several steps. Firstly, various concentrations of PbI_2 dissolved in DMF were spin-coated on the plasma treated FTO glass with 2000 rpm 40 sec. During the PbI_2 coating, different concentration of histidine iodide or histamine iodide methanol solutions were prepared at 60°C . After the coating, the PbI_2 substrates were located in the furnace to maintain at 60°C . When the temperature of substrates was stable, the substrates were submerged in the prepared methanol organic solution for 5 min at the same temperature. Color change was observed. After the dipping, the synthesized OIPs film was dried in nitrogen atmosphere.

2.3 Characterization

2.3.1 Scanning electron microscopy (SEM)

PbI_2 and crystallized HPI, hPI powder samples were visualized as deposits on Si with a field emission scanning electron microscope (Merlin compact, Zeiss). Before the powder images were acquired, Pt sputtering was conducted at 10mA for 1 min, (Cressington 108 Auto, Zeol) and silver paste were used to fix the samples on the holders. After this, we dried the samples for 12 hours. Sectional images were taken using a section holder on the same instrument. An acceleration voltage was 1.0 kV at different scales.

2.3.2 X-ray diffraction

2.3.2.1 Powder, Film X-ray diffraction

Powder and film X-ray diffraction were measured on D8 Advance X-ray diffractometer. The source of X-ray was $K\alpha$ radiation from Cu (wavelength = 1.54056 Å) Powder OIPs samples were prepared by drying at 100 °C, and loaded on Si holder. In contrast to the powder, film samples were prepared by coating on FTO glass. The X-ray pattern was measured from 3° to 83° with a rate of 5°/min, and a step of 0.02°. We compared the extrapolated data to the reported data based on JCPDS cards.

2.3.2.2 Single crystal X-ray diffraction and Synchrotron

Single crystal XRD data was measured on crystal XRD analyzer. (D8 Venture with dual source, Bruker AXS) Prior to our analysis, purified single crystals were optically tested under a microscope to determine the viability of high quality XRD pattern. Well-grown single crystal was captured by loop and located in the X-ray chamber at 293 K with Micro-Cu X-ray source. Collected XRD data was solved by XS structure solution program using direct methods. In addition, data were refined using least square minimization. To visualize crystal structure, Olex 2 program was utilized.

Synchrotron analysis was conducted in beam-line of 2D-SMC at Pohang accelerator laboratory. X-ray source with bending magnet had 3.0 GeV, and

its resolution was 10^{-4} . The intensity and beam size were 10^{11} photons/sec and 0.1 mm by 0.1 mm, respectively. Measured XRD pattern was detected by ADSC Quantum 210 CCD detector and solved in the same program as we introduced in single crystal XRD analysis.

2.3.3 Thermogravimetry (TGA)

Thermal stability of HPI and hPI was measured by TGA using Q 5000 V 3.5 model. 10 mg of samples was analyzed from room temperature to 600°C . To avoid oxidation, we measured TGA under nitrogen atmosphere. The rate of increasing temperature was $10^{\circ}\text{C}/\text{min}$.

2.3.4 Band structure

2.3.4.1 Reflectance and Absorbance measurement

Reflectance and absorbance were collected from Cary-500 spectrophotometer (Agilent Technologies) with a range of 300 nm ~ 1400 nm which is infra-red and visible light region. Powder HPI and hPI were loaded into the holder, and measured by the diffuse mode through the integrating sphere. For the calibration, we measured the blank reference to get rid of errors before we get the data.

2.3.4.2 Ultraviolet photoelectron spectroscopy (UPS)

For loading on UPS, HPI and hPI were coated on 1cm by 1cm of Si wafer at 2000 rpm 40 sec. After the coating, samples were dried at 100 °C for 40 min. We applied -8.86 V of bias as back contact voltage which was calibrated in obtained data. Beam size of UPS was 15 μm and its penetration depth was less than 50 nm. The measuring energy was calculated based on He I photon energy which has 21.2 eV from the vacuum level.

2.3.5 Photocurrent measurement

For screening the photoactivity and measuring photocurrent, we set up the minute fabrication method. To remove the error current, 0.15M titanium diisopropoxide bis(acetylacetonate) ($[(\text{CH}_3)_2\text{CHO}]_2\text{Ti}(\text{C}_5\text{H}_7\text{O}_2)_2$) in 1-butanol solution was coated on FTO by spin coating at 4000 rpm 40 sec. After the coating, we heated up the substrates in the furnace at 500 °C for 30 min. During this process, thin layer of TiO₂ film was formed onto the FTO glass. When the TiO₂-FTO glass is prepared, HPI or hPI was coated on the substrate for 2000 rpm 40 sec. For fabricating electrodes, we used thermal evaporator (ULTECH) to make 100 nm of gold electrode on perovskites coating.

Fabricated samples were measured by the probe station (MS Tech) as two

point contact method. We applied the voltage from 100 μV to few tens of voltages to detect the generated current. For identifying the light response, coated perovskites samples were held for 120 sec under 300 W of Xenon lamps (Newport) with 760 nm filter. After the holding, light was turned on and off several times for 1 min per each step. During the light blinking, photocurrent was measured at the constant voltage.

2.3.6 Photovoltaics measurement

The photovoltaic properties were measured using a potentiostat. (CHI 608C, CH instruments) Additionally, to get the I-V plot of DSSCs, we used solar simulator under AM 1.5, 100 mW/cm^2 . (PECL 11, Peccell) We chose the best data among deposited four electrodes on OIPs coating. J_{SC} , V_{OC} , fill factor, and efficiency were calculated by photo-analyzer program.

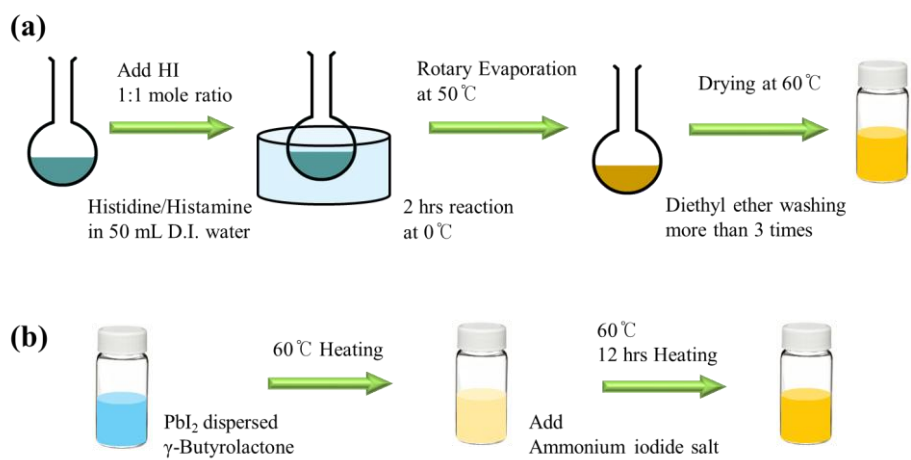


Figure 2.1 Schematic of (a) imidazolium iodide synthesis and (b) OIPs synthesis

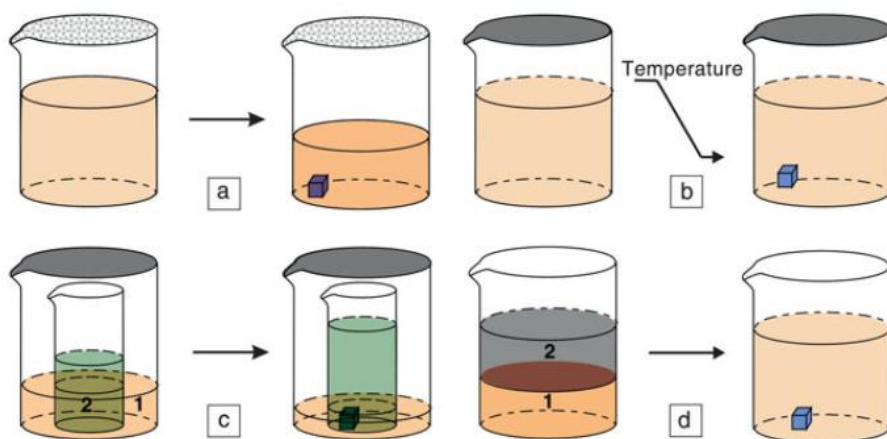


Figure 2.2 Various methods of single crystal preparation in solution. (a) Solvent evaporation method, (b) slow-cooling method, (c) vapor diffusion method, and (d) liquid-liquid diffusion method. We used (c) method for HPI single crystal, and (b) method for hPI single crystal. In (c) process, the solvent 1 was acetonitrile (volatile, insoluble), and the solution 2 was HPI-DMF solution.⁸⁵

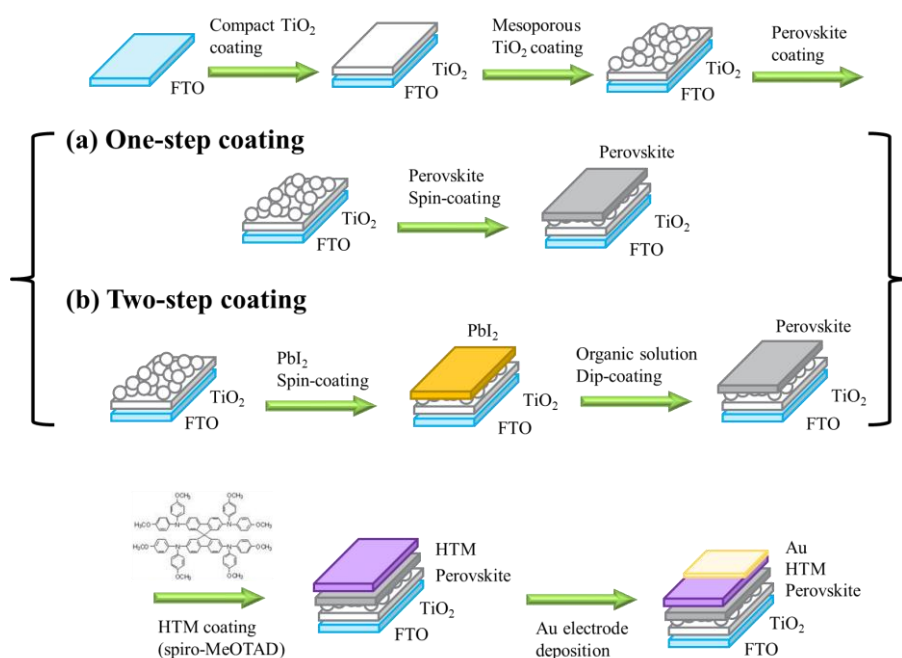


Figure 2.3 Schematic of solid-state perovskite cells fabrication. (a) One-step spin-coating, (b) two-step dip-coating.

Chapter 3. Results and Discussions

3.1 Structure and properties characterization

3.1.1 Crystal structure determination

By calculating the tolerance factor (explained in chapter 1.1.2), it was possible to predict that synthesized HPI and hPI crystals should be 2-dimensional OIPs. (A_2BPbI_4) In other words, inorganic layers of PbI_4 and organic layers of histidine or histamine packed as alternating layer-by-layer. Additionally, synthesized histidine and histamine salts are dication salts which contain two binding sites interacting with inorganic layers with two of additional protons and the same number of iodide ions. In this point of view, we could estimate the molecular formula of each perovskites. HPI should be $(C_6H_{11}N_3O_2)PbI_4$, and hPI should be $(C_5H_{11}N_3)PbI_4$ which means the organic salt was reacted with PbI_2 as 1:1 ratio.

For determination of crystal structure, we preliminarily investigated SEM images. PbI_2 powders had no regular ordering, and the size was about 30 μm . Otherwise, synthesized HPI and hPI had its own crystal morphologies: HPI was diamond shape, and hPI was rectangular shape. Through SEM images, we found that the crystal morphology of our new OIPs and precursor PbI_2 were different. In addition, we confirmed that both HPI and hPI were well-synthesized in a right way. (Figure 3.1)

After the preliminary examination by SEM images, we analyzed X-ray

diffraction (XRD) pattern in detail. As-synthesized OIPs powder was simply analyzed by powder XRD, however, it is hard to determine the original crystal structure of HPI and hPI. Therefore, both high quality single crystal XRD pattern and computational calculation were needed to find out what kind of crystal system they have. In this chapter 3.1.1, we successfully discovered hPI first. This report is worth noting as it is the first crystallographic discovery of hPI in the world. In the case of HPI, high quality of single crystal is hard to be prepared due to its carboxylic group in histidine. The hydrogen bond of carboxylic acids may act as a barrier to get perfect crystal. For this reason, we analyze hPI first in this research. The crystal structure of HPI will be solved in our next work.

3.1.1.1 Analysis of as-synthesized OIPs powder

The as-synthesized OIPs powder was prepared by drying up solvent at 100 °C. Collected HPI and hPI powders displayed different XRD pattern compared to PbI₂ precursor. (Figure 3.2) It means that HPI and hPI have their own phase, and they are totally different with PbI₂. In the case of HPI, two big characteristic peaks could be observed at 22.5° and 28.5°. In comparison, hPI showed one characteristic peak was observed at 28.0°. The additional characteristic peak located under 10° indicates the interlayer distance between inorganic layer and organic layer in 2-dimensional OIPs structure.⁸⁶ In detail, this distance is identical to lattice parameter *c* by crystallography. By comparing the peak position and intensity of these

characteristic peaks, we could analyze how much perovskites are formed or if they are synthesized or not.

3.1.1.2 Computational analysis of single crystal

From the diffraction pattern from synchrotron, we solved the crystal structure of hPI. R1 value was 3.38%, and completeness was 87%. The coordination of hydrogen atoms were calculated by considering electron density.

Solved hPI crystal has monoclinic, 2-dimensional <100>-oriented structure whose space group is $P2_1/c$. In addition, the chemical formula is $(C_5H_{11}N_3)PbI_4$, indicating that the histamine molecule and PbI_2 are combined as 1:1 ration. In table 1, the lattice parameters and crystal factors are summarized. Interestingly, our hPI structure has β as 92.11° . It indicates that the crystal structure is almost b-elongated tetragonal structure that has rectangular morphology. This is tantamount to the result that we have reported in SEM image analysis.

In figure 3.1, visualized hPI crystal building block is represented. PbI_6 octahedrons are well-constructed as corner-shared distorted structure. Among these inorganic layers, histamine dications with two protonated nitrogen atoms intervene into PbI_6 layers. Alternation of imidazole-amine in the crystal, and alignment of alkyl chain are also observed.

When we focus on inorganic layer, we can find out the distortion. The bond lengths between lead and iodide in PbI_6 octahedron are approximately

from 3.156 Å to 3.201 Å, while the bond angles of I-Pb-I vary from 83.5° to 94.75° which means they are substantially 90°, with some strains in it. More interestingly, the bond angles of Pb-I-Pb fluctuating around 153.86° signifying that PbI_6 octahedrons are not aligned in the same plane. This alternating zigzag structure is an indication that either deviation or corrugation has been generated in PbI_6 inorganic layer. Interaction between the lone pairs in electron-abundant lead atom engenders this corrugation.⁸⁷ Not only the deviation, but also the rotation of PbI_6 octahedron along a-and b-axis is observed. (Figure 3.5) We think that the distortion and rotation may generate the unique hPI crystal system and optical properties. All bond lengths and angles are summarized in table 2.

In the case of histamine organic layer, it is revealed that both protonated imidazole ring and primary ammonium cation generate its peculiarity. In most previous OIPs research, only primary amine of alkyl chain could plug into inorganic layers. However, we discover that the whole aromatic imidazole ring can directly interact with PbI_4 inorganic layer. Otherwise, the interaction between primary amine and inorganic layer demonstrate its verisimilitude with precedent alkyl chain interaction as benzyl amine or phenethylene amine. The bond lengths of C-C vary from 1.48 Å to 1.51 Å, otherwise the angles of C-C-C vary from 109.6° to 111.8°. It means that histamine molecules have low angle strain and high thermodynamic stability.

One of the most important binding factors in organic-inorganic interaction is halogen bonding. (Figure 3.4) Halogen bonding is the interaction between positive (+) charge of hydrogen and negative (-) charge of halide. As we can

see in figure 3.4, hydrogen atom of amine group (N2) takes close position to neighboring iodide ions (I5, I6, IA) to make amine group attract iodide ion. The distances of N-H-I are 2.797 Å, 2.937 Å, and 2.999 Å. In addition the bond angles of N-H-I are from 164.42° to 144.25°. On the other hand, hydrogen atoms in imidazole ring also locate between aromatic nitrogen atoms (N3, N4) and I4 iodide ions to make the halogen bonding. The bond lengths of N-H-I are 2.654 Å (159.80°), and 2.716 Å (150.19°), respectively.

Bond lengths and angles indicate that there is secondary bonding, because the bond length of halogen bond is less than 3.0 Å in general. The most interesting fact is that the average bond length between imidazole and iodide (2.68 Å) is shorter than that of amine and iodide. (2.92 Å) Based on chemical approach, the short length means the strong halogen bond. Scientifically, the basicity of imidazole ring (sp^2 nitrogen) is lower than primary amine. (sp^3 nitrogen) Therefore, electron donation from nitrogen atom to hydrogen atom is weaker in imidazole with a concept of Lewis base and s-character. This makes hydrogen in imidazole more positive. Consequently, hPI structure is possibly stable compared to MPI and ordinary amine-based OIPs. Unique water-stability of HPI and hPI can be explained at this viewpoint.

In addition, imidazole ring and primary amine make electrostatic interaction with inorganic layers. Especially, in the case of imidazole, electrostatic force has important role due to its steric hindrance. Steric hindrance can be observed through the bridging Pb-I bond. For example,

binding direction of lead and four of its neighboring iodide ion is opened up outwards, and the bond length between Pb1-imidazole (5.91 Å) is longer than Pb1-primary amine. (4.59 Å) Also, the case of bond angle is similar: distortion of Pb-I-Pb around imidazole (206.2°) is larger than that of Pb-I-Pb around primary amine. (177.0°) This is because of the size of imidazole molecule.

Our hPI crystal system is different with reported MPI. By calculating tolerance factor of MPI, it has 3D perovskite structure. Small size of whole methyl ammonium cation can be possessed into PbI_6 octahedron lattice with only little elongation. However, hPI perovskite has 2D structure based on the tolerance factor. Only nitrogen-connected hydrogen atoms plug into the inorganic layer, and left organic chains are located in the gap between inorganic layers.

Compared to the previous work about histamine lead bromide ($(\text{C}_5\text{H}_{11}\text{N}_3)_2\text{PbBr}_4$ (hPBr) whose crystal structure was recognized as $P2_1/c$, our new imidazole-based OIP also has same crystal structure.⁸⁸ Both imidazole ring and primary amine also interact with inorganic layer in this structure. However, because of the size of halide ion, histamine has more extended structure. hPBr has (1) different lattice parameters, (2) different histamine distortions, and (3) different halogen bond positions compared to hPI. The value of lattice parameters of hPBr are $a = 10.632 \text{ \AA}$, $b = 11.617 \text{ \AA}$, $c = 11.955 \text{ \AA}$, $\alpha = 90^\circ$, $\beta = 110.059^\circ$, and $\gamma = 90^\circ$. When we compare these values with table 1, hPBr has more monoclinic-like structure with larger a , c , and angle β . (110.059° for bromide system, 92.11° for iodide system)

Moreover, histamine lead bromide has shorter bond length (2.93 Å ~ 3.07 Å) compared to that of lead iodide system. (3.06 Å ~ 3.30 Å) This phenomenon is stemmed from Pb-Br distance. With the same reason, lattice volume is bigger in hPI. However the density of hPI lattice is higher than hPBr. This means the atomic weight change from hPBr to hPI is larger than the volume change because of halide ions. (I = 126.9, Br = 79.9) Lattice distortion also causes angle strain of histamine molecule. hPBr has higher angle strain than hPI, because angle of C-C-C in hPBr is 112.6° (averaged) is larger than that of hPI. (110.7°, averaged) In addition, halogen bonding sites are completely different: histamine molecules interact with two axial bromides and one equatorial bromide in hPBr, while they interact with one axial iodide and two equatorial iodides in hPI,

As well as hPBr, hPI has a different structure compared to several OIPs.⁸⁹
⁹⁰ N-(3-aminopropyl) imidazole lead bromide has <110>-oriented 2-dimensional structure, and contains only one halogen bond. On the other hand, Propyl-3-methyl imidazole lead bromide has 1-dimensional aligned inorganic structure. In this case, the organic molecules do not have the hydrogen atom so that there is no halogen bond. Due to its low interaction between organic and inorganic segment, unstable PbBr₆ cannot make complete octahedron. These different OIPs mean that different length or functional group of organic chain can distort inorganic framework. In other words, organic molecules in OIPs can template inorganic sheets.

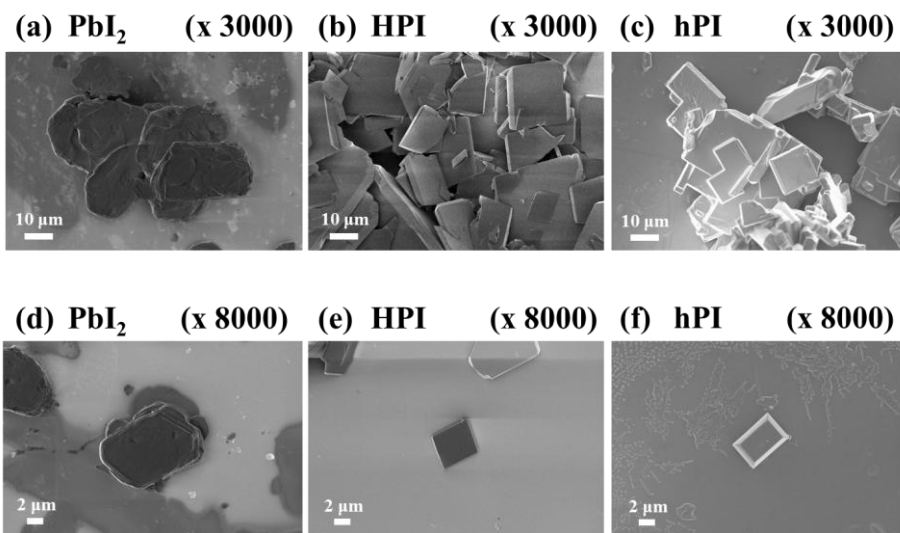


Figure 3.1 SEM images of (a), (d) PbI_2 , (b), (e) HPI and (c), (f) hPI crystal. (d), (e), (f) images are enlarged images as x 8000. Compared to PbI_2 , the crystal morphology of HPI was diamond, and hPI was rectangle.

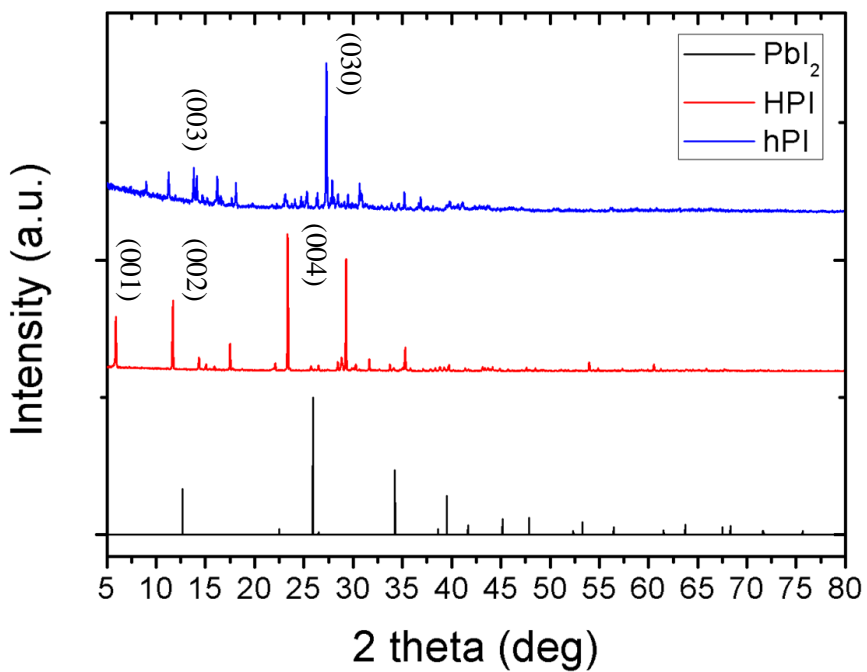


Figure 3.2 Powder XRD pattern of PbI_2 precursor, HPI, and hPI. Compared to PbI_2 , HPI and hPI had their own peak position. HPI characteristic peaks located at 22.5° and 28.5° , while hPI characteristic peak located at 28.0° . Plane directions are noted on the plot.

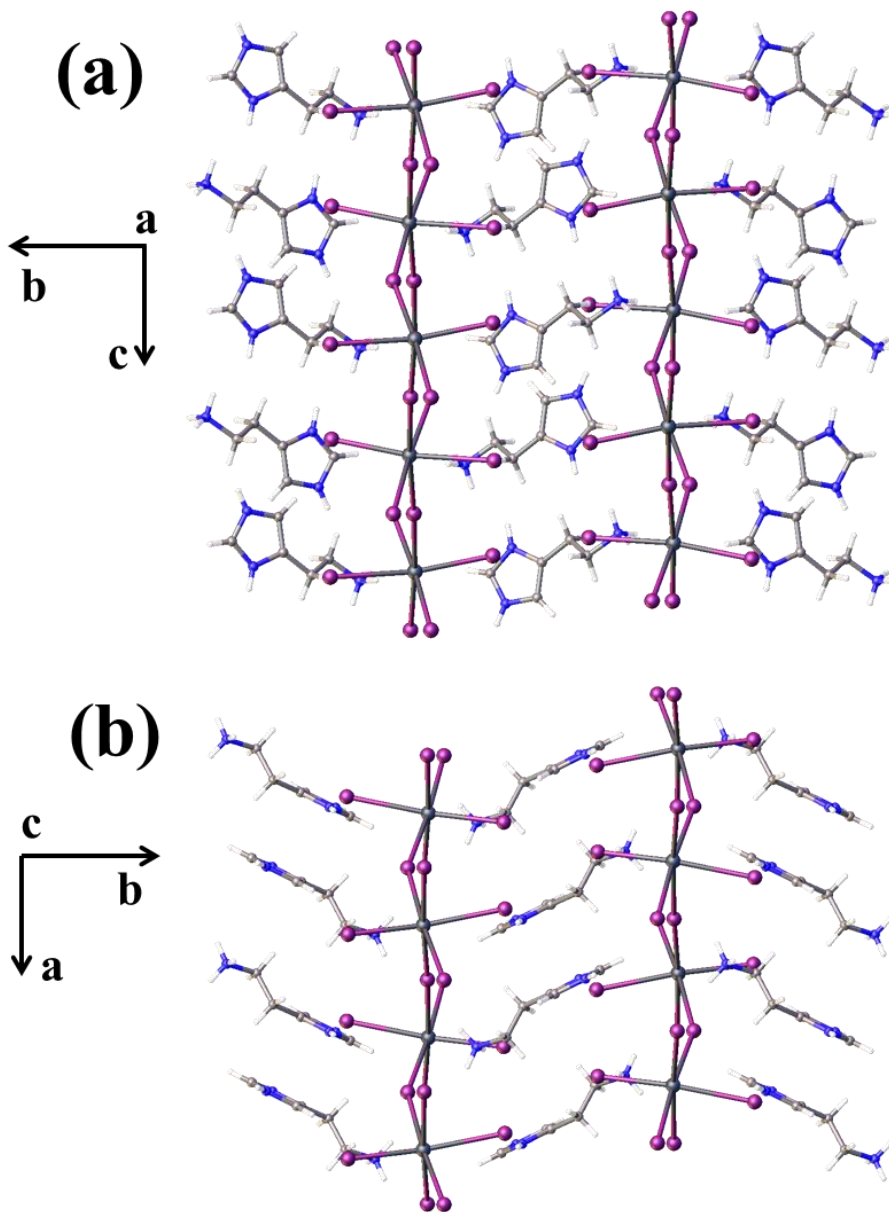


Figure 3.3 Images of hPI single crystal structure along (a) (100)-direction, and (b) (001)-direction

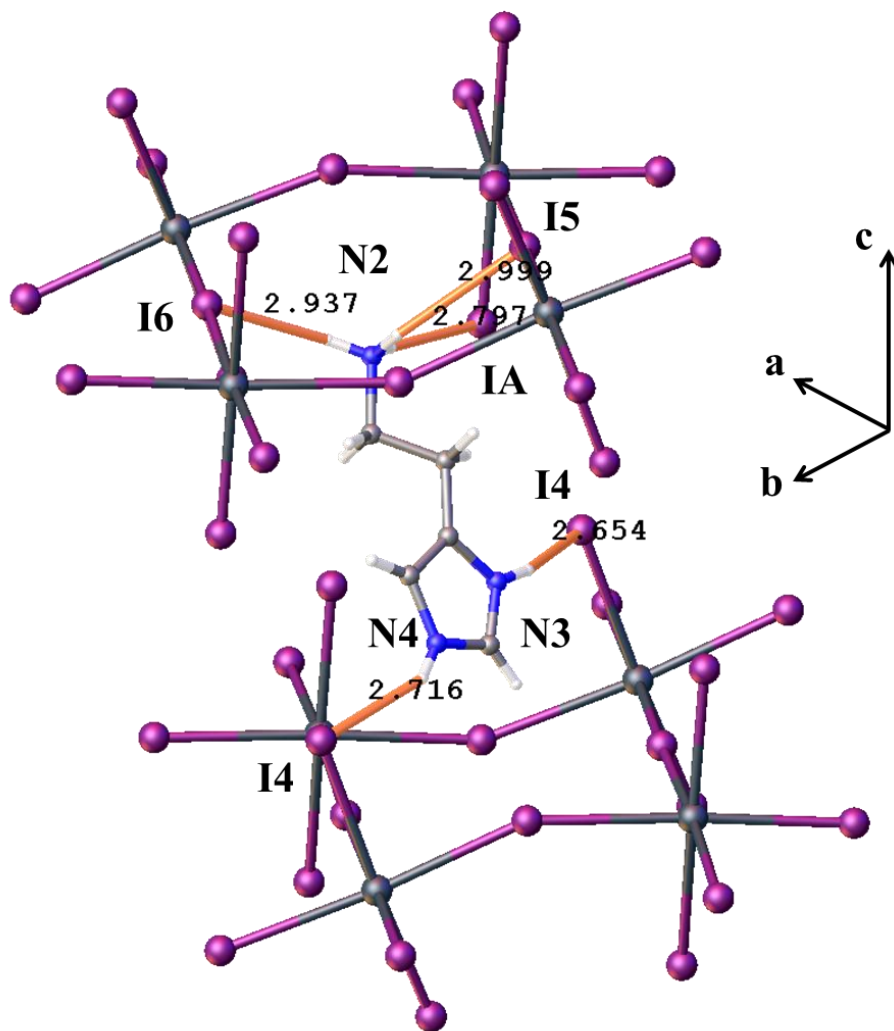


Figure 3.4 Halogen bonds between protonated histamine and iodides in PbI₆ octahedrons. The strong bond strength stabilizes hPI perovskite structure. Interestingly, not only primary amine, but also whole imidazole ring interacts with inorganic layer.

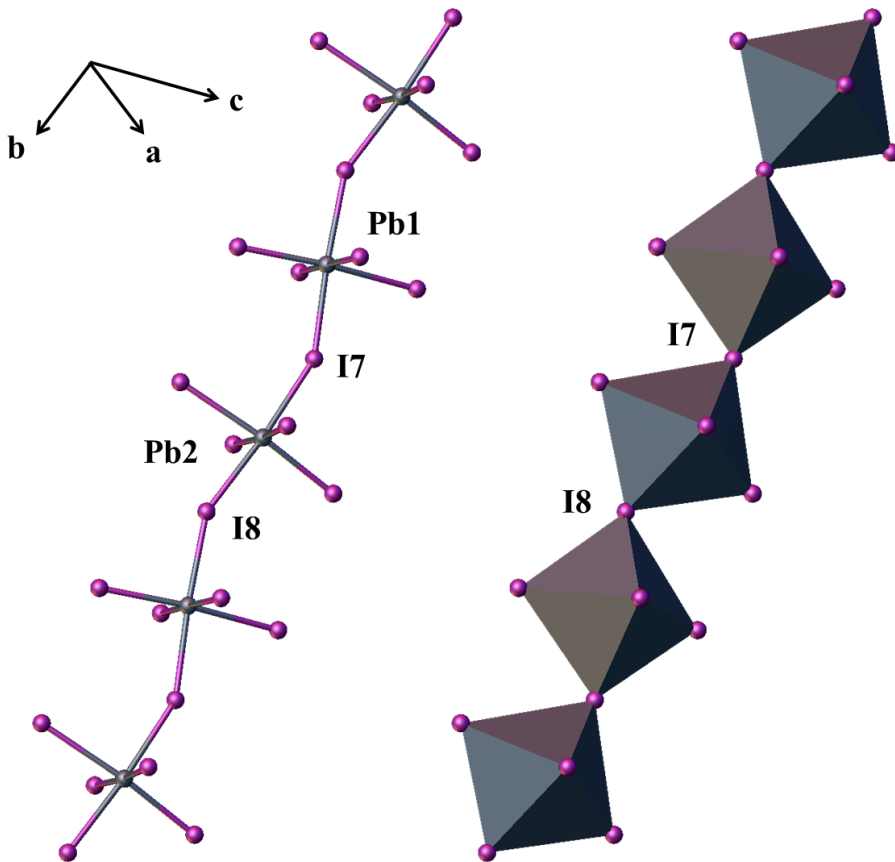


Figure 3.5 Corrugated structure of PbI_6 octahedron chain with I7-I8 corner-sharing. This corrugation makes bond length and angle distortion.

Table 1. Crystal data for hPI compared to hPBr

	hPI	hPBr
Formula	(C ₅ H ₁₁ N ₃)PbI ₄	(C ₅ H ₁₁ N ₃)PbBr ₄
M.W.	1655.92	640.00
Crystal system	Monoclinic	Monoclinic
Space group	P2 ₁ /c	P2 ₁ /c
a (Å)	8.902	10.632
b (Å)	19.756	11.617
c (Å)	8.933	11.955
α (°)	90	90
β (°)	92.11	110.059
γ (°)	90	90
Volume (Å ³)	1570.0	1387.0
Z	2	4
ρ (mg/mm ³)	3.503	3.065
F (000)	1424	1136
R ₁ , ωR ₂ (I>2σ)	0.0338, 0.0913	0.0453, 0.1008

Table 2. Selected bond distances (Å) and bond angles (°) of hPI

Bond length (Å)				
C1 C7	1.512(6)	I2 Pb1	3.2985(7)	
C1 N3	1.501(6)	I3 Pb1	3.2546(10)	
C5 C7	1.484(6)	I3 Pb1	3.1714(10)	
C5 C8	1.366(6)	I4 Pb1	3.2005(10)	
C5 N4	1.384(6)	I4 Pb1	3.1564(9)	
C8 N6	1.367(7)	I5 Pb1	3.0593(7)	
C9 N4	1.328(6)	Pb1 I3	3.2546(10)	
C9 N6	1.329(7)	Pb1 I4	3.1565(9)	
Bond angle (°)				
N3 C1 C7	109.6(4)	I3 Pb1 I3	175.898(8)	
C8 C5 C7	133.2(4)	I3 Pb1 I4	90.015(18)	
C8 C5 N4	105.7(4)	I4 Pb1 I2	85.356(12)	
N4 C5 C7	121.1(4)	I4 Pb1 I2	90.617(11)	
C5 C7 C1	111.8(4)	I4 Pb1 I3	88.835(18)	
C5 C8 N6	107.1(4)	I4 Pb1 I3	89.946(18)	
N4 C9 N6	107.4(5)	I4 Pb1 I3	90.929(17)	
Pb1 I3 Pb1	177.027(13)	I4 Pb1 I4	175.900(7)	
Pb1 I4 Pb1	153.821(14)	I5 Pb1 I2	170.717(10)	
C9 N4 C5	109.9(4)	I5 Pb1 I3	87.437(10)	
C9 N6 C8	109.9(4)	I5 Pb1 I3	96.533(11)	
I3 Pb1 I2	83.614(8)	I5 Pb1 I4	92.190(13)	
I3 Pb1 I2	92.462(10)	I5 Pb1 I4	91.666(12)	

3.1.2 Optical properties characterization

In comparison to the precedent cases with $\text{CH}_3\text{NH}_3\text{PbI}_3$ (MPI) structure, the new type of imidazole-based OIPs manifested eccentric optical properties. Histidine lead iodide (HPI) has a thick red color, and histamine lead iodide (hPI) has a dark orange color, while MPI only has grey or dark brown color. The color has intimate connection to the band gap energy, which means that our new perovskites structures have the different band gap energy to MPI. There scarcely exist research for tuning the color of OIPs, however, we successfully have changed not only the color, but also the band gap energy. It is the first report to change the band gap energy dramatically using organic chain variation in visible light region. For a wide range of visible light absorption, this new adjustable perovskites have potential to use as photosensitizer in various wavelengths.

Figure 3.6 shows the reflectance and absorption spectra of HPI and hPI in detail. From the spectra, we found that HPI and hPI absorb the wide range of visible light except the long wavelength. HPI absorbs much more light in visible light region, otherwise hPI absorbs about 10% of more light in infra-red region from 600 nm to 1000 nm. As a result, the color of HPI is thicker than that of hPI. Although the absorption spectra from diffuse mode reflectance carried negligible errors from transmittance value, it is possible to calculate the approximate maximum absorption wavelength that HPI is 610 nm and hPI is 550 nm, respectively.⁹¹

3.1.3 Band gap energy and band position determination

As we mentioned in chapter 3.1.2, the band gap energy is related with the optical properties. Although there are many methods to calculate the band gap energy, we chose a widely-used method in perovskites research field. From the reflectance data, we could get the Kubelka-Munk transformation for measuring optical band gap. $F(R)$, the optical absorption coefficient, was calculated as $F(R) = (1 - R)^2 / 2R$, that R value stands for the percentage of reflected light from reflectance data. After then, we plotted the transformed function of Kubelka-Munk formula that can be expressed as $[F(R) hv]^p = k (hv - E_g)$. hv is the incident energy of photon, k is constant related with the photon transition, p is the power index depending on the band gap structure, and E_g is the band gap energy. If we focus on the power index p , it is 0.5 when the materials have indirect band gap structure, while it is 2 when it is the direct band gap structure.⁹²

Transformed Kubelka-Munk diagrams of HPI and hPI are expressed in figure 3.7. The red line indicates the linear extrapolation of original transformed blue line. As we assumed that our new perovskites absorb the light through the direct band gap structure, the power index p was set as 2. From the result of Kubelka-Munk analysis, band gap energy of HPI was determined as 2.04 eV (607 nm), and that of hPI was determined as 2.23 eV (556 nm) These values were well-matched with absorption spectra in the point of maximum absorbing wavelength.

Compared to the band gap energy of MPI in previous work, (1.50 eV) our imidazole-based perovskites have wider gap. Consequently, the color of MPI is dark grey absorbing a wide range of visible light from 820 nm. When we focus on the huge portion of visible light in solar power, our imidazole-based HPI and hPI is less photo-responsible than MPI. However, yet our new OIPs showed the most outstanding absorption spectra via other lead-based 2D perovskites reported in previous research. The color of HPI and hPI was red and orange respectively. It means that HPI and hPI absorb most of visible light except long wavelength of red light.

To determine the maximum state of valence band, we measured UPS. (Figure 3.8) PbI_2 precursor, synthesized HPI and hPI were measured. To find out the valence band position, we needed three values. One is that applied energy transformed into He I, (21.2 eV) another is secondary cut off energy extrapolated from the high energy curve in the plot. The other is Fermi edge energy extrapolated from the low binding energy region which means the band edge of the valence band.⁹³ Extrapolation was calculated with linear approximation as a statistical way. To get the value of valence band position, the width of the spectra should be withdrawn from the applied energy. In other word, the gap between secondary cut off energy and Fermi edge energy should be subtracted by the He I energy which is 21.2 eV.

The binding energies of secondary cut off point were 18.1 eV for PbI_2 , 17.8 eV for HPI, and 17.4 eV for hPI. On the other hand, the binding energies of Fermi edge point were 2.35 eV for PbI_2 , 2.95 eV for HPI and 1.90 eV for hPI. From the calculated values, it was possible to estimate the

valence band position: -5.45 eV (PbI₂), -6.35 eV (HPI), and -5.70 eV (hPI) below the vacuum level, respectively. Based on the valence band, conduction band position also could be estimated by the result of band gap energy: -3.15 eV for PbI₂, -4.31 eV for HPI and -3.57 eV for hPI.

For a comparison, we sketched the band gap energy and the position of valence band of each material as a schematic diagram in figure 3.9. Compared to the previous reported band structure of MPI, estimated valence band of our new OIPs is located at a lower position, especially HPI. Through the band alignment, we could select the candidate for the sensitizer in solid-state DSSCs. It will be discussed in chapter 3.3.2.

3.1.4 Thermal stability characterization

OIPs Thermal stability data is necessary to examine the limiting temperature for DSSCs fabrication process. Most of OIPs, they are easily degradable in few hundreds of Celsius degree because of their organic chain.

Our new imidazole-based OIPs, HPI and hPI, showed two-step degradation. The first decomposition step was proceeding because of organic iodide degradation to original amine and hydriodic acid.⁹⁴ After that, the second step was proceeding by degradation of whole organic molecules with losing hydriodic acid from OIPs lattice. Decomposition of organic molecules was complicated, because there is thermally stable aromatic imidazole ring. Alkyl chains were decomposed at the first time, and then thermally stable

aromatic imidazole group was decomposed. Mass loss was also dependent on the material purity.

From TGA analysis, HPI structure lost 6.40 % of its weight at 262.8 °C, and 23.31 % of its weight at 345.5 °C. The color was changed from red to black because of the degradation of histidine at this transition point. In the case of hPI, 30 % of weight loss was occurred at 315.8 °C, and 54.5 % of weight loss was occurred at 506.9 °C. In figure 3.10, we expressed not only the original TGA curve, but also the first derivatives curve to emphasize when the perovskites are started to break down and how much they are degraded.

Compared to one step degradation of MPI at 280 °C, HPI is thermally unstable compared to MPI. Otherwise, hPI is much stable than MPI. The lack of harbinger during the TGA analysis impeded/disabled the detection of phase transition. The reason for this is that there is no chemical reaction in the structural change, signifying that it is a second order transition to lower symmetry.⁹⁵

To sum it up, until the temperature reaches 310 °C, hPI perovskites remains stable, and it is more thermally durable than MPI and HPI perovskites whose degradation was started around 280 °C and 260 °C, respectively. Based on this TGA data, we concluded that both of perovskites should be treated under 260 °C during the DSSCs fabrication and preheating for coating.

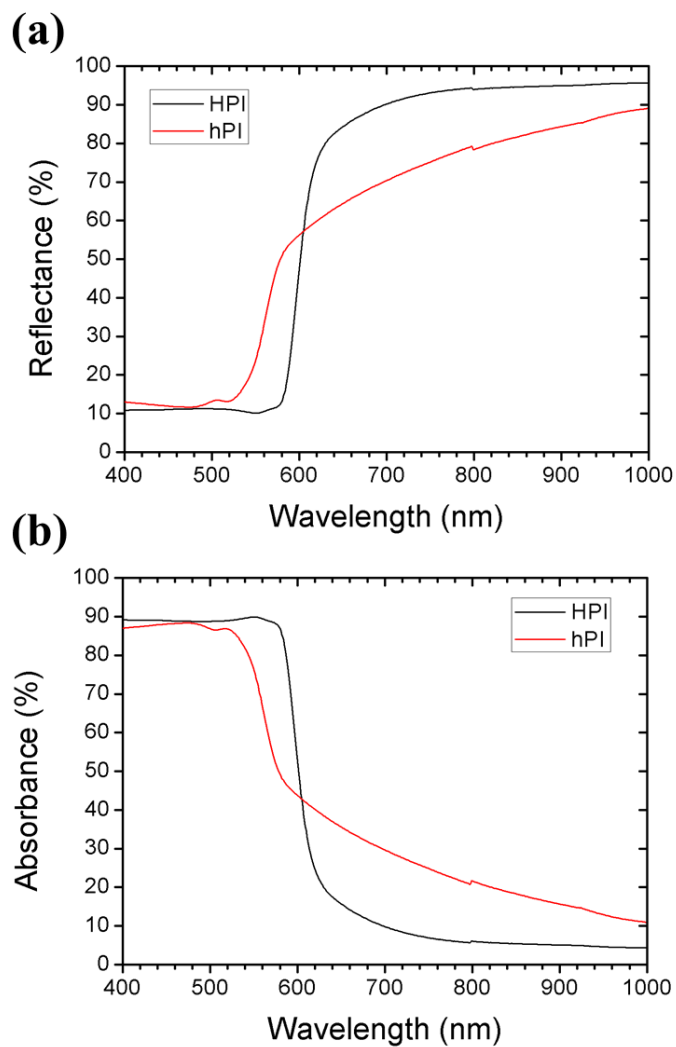


Figure 3.6 (a) Diffuse mode reflectance plot of HPI and hPI. (b) Absorption spectra of HPI and hPI. Light absorption of HPI was larger than hPI, so that HPI had dark red color, and hPI had orange color.

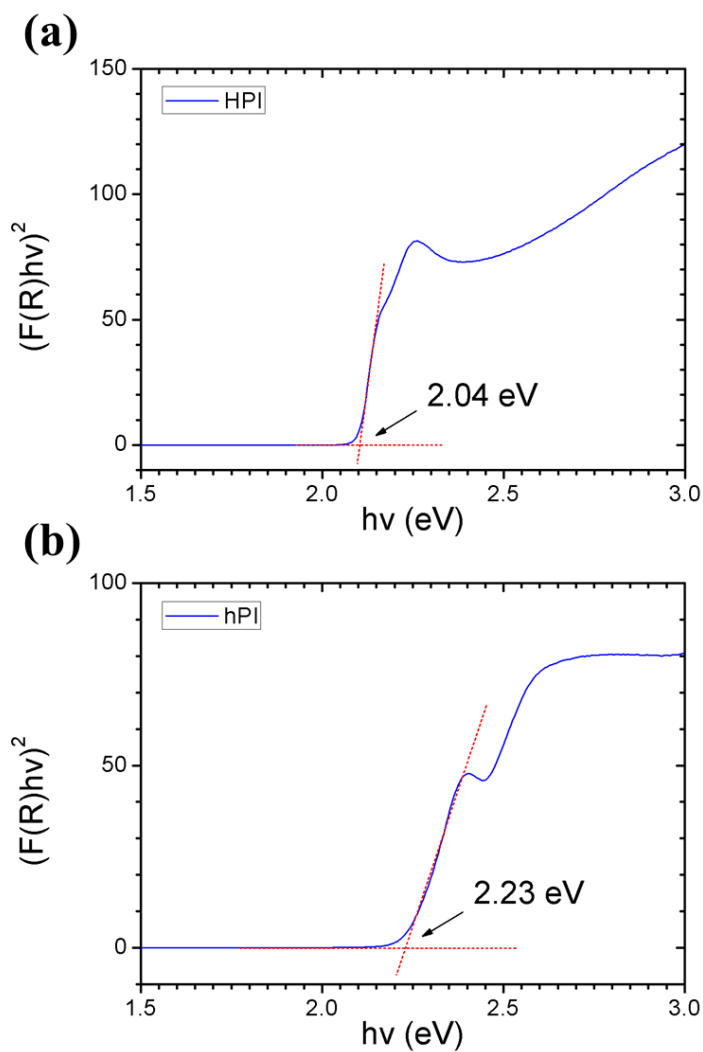


Figure 3.7 Kubelka-Munk diagrams of (a) HPI and (b) hPI for determination of band gap energy. The red line means the linear extrapolation. Calculated band gap energy was 2.04 eV for HPI, and 2.23 eV for hPI, respectively.

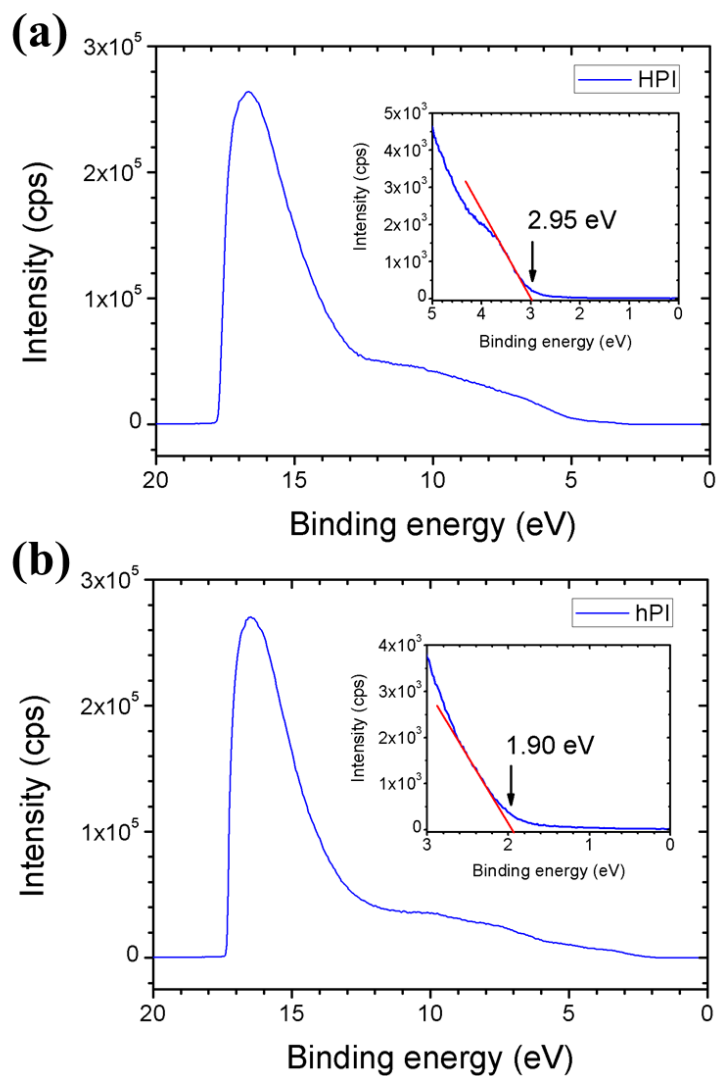


Figure 3.8 UPS spectra of (a) HPI and (b) hPI. The red line indicates linear extrapolation to find out the Fermi edge energy level. Valence band energy was calculated as -6.35 eV for HPI and -5.70 eV for hPI by subtracting to He I energy. (21.2 eV)

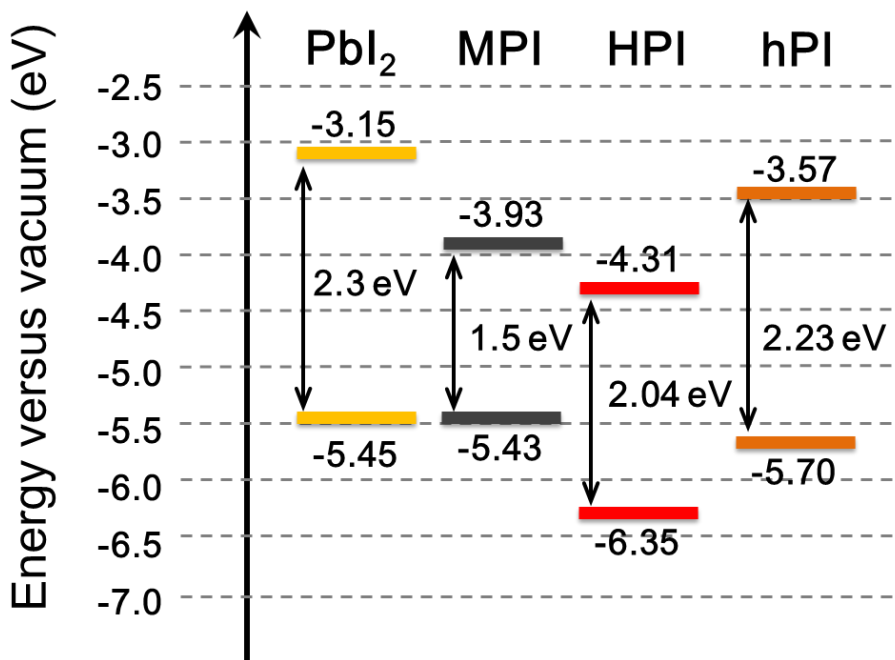


Figure 3.9 Schematic band structure of PbI₂, MPI, HPI, and hPI. Compared to MPI, HPI and hPI have lower valence band position and larger band gap energy. The color of graph indicates the color of perovskite. The band structure of MPI is based on the reference.

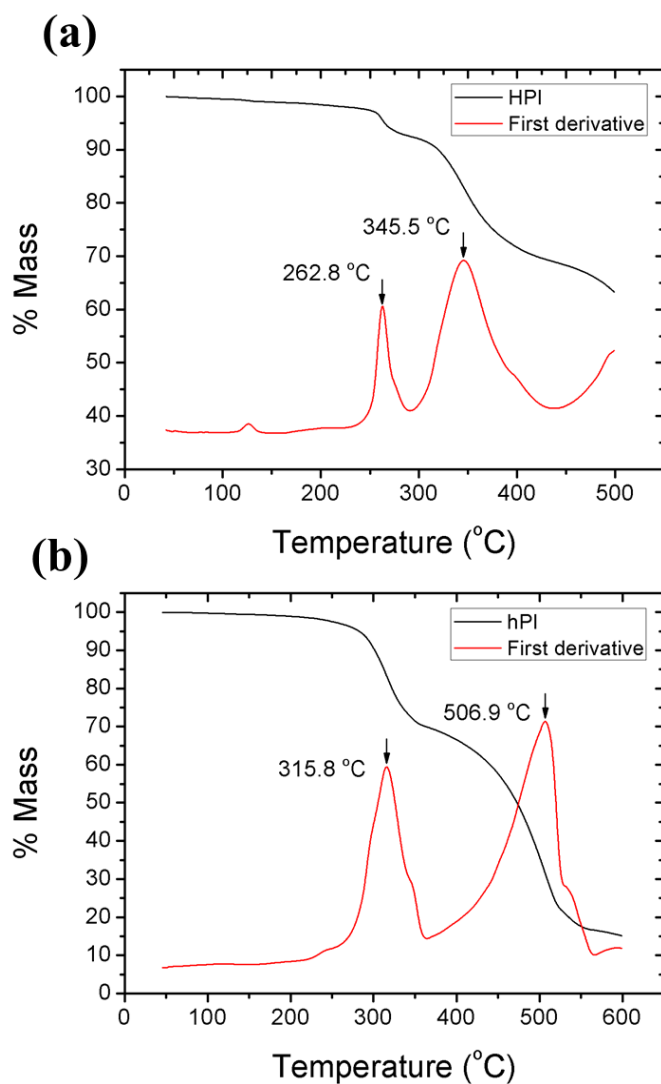


Figure 3.10 TGA data of (a) HPI and (b) hPI. Two-step degradation was observed. Synthesized HPI was stable until 262°C, otherwise hPI was stable until 315°C. In fact, hPI was more thermally stable than HPI.

3.2 Coating dependence and optimization

3.2.1 One-step coating

For one-step spin-coating, we have to make homogeneous solution in appropriate solvent. However, HPI could not generate homogenous solution. HPI crystals were precipitated in γ -butyrolactone. On the other hand, they were soluble in DMF. However, the coating was not formed in this case: only crystallization occurred in certain position on substrate like islands. Without good solvent for HPI spin-coating, it was impossible to coat HPI as an one-step on the substrate. Because of this problem, the one-step coating was performed only for hPI.

In this chapter, we changed variables for optimizing hPI spin-coating; solution concentration, organic solvent, and pre-treatment. Following chapters supported what is the maximized condition for uniform hPI coating. The substrate was FTO glass, and the standard conditions were 2000 rpm 40 sec. Reacting temperature was 60°C in γ -butyrolactone.

3.2.1.1 Concentration dependence

First of all, we set the concentration variables. The maximum solubility of hPI in γ -butyrolactone is around 30 wt%, so that we evaluated 10 wt%, 20 wt%, 30 wt%, and 40 wt% each. As a result, the surface morphology of hPI

coating was not so different depending on the concentration. However, the thickness was different confirmed by section imaging by SEM. From 10 wt% to 40 wt%, the thickness varied from 49.9 nm to 343.0 nm. These values were summarized in figure 3.11. We chose less than five different thickness data, and averaged statistically due to the low uniformity of hPI coating.

3.2.1.2 Organic solvent dependence

In previous study, MPI was coated homogeneously on ITO substrate with DMF better than γ -butyrolactone. The size of domain size in DMF was smaller than that of γ -butyrolactone. Although both coating were not uniform, DMF coating with relatively large contact area was beneficial to improve the charge transportation and the efficiency for solar cells.

Similarly, based on the organic solvent dependence of MPI, we got insight and focused on the trend of hPI coating relying on solvents. We found out that hPI solution could be homogeneous in DMSO, DMF and γ -butyrolactone. However, DMSO could intervene to the PbI_2 lattice to form yellow needle-shaped crystal at low temperature. The sulfur atom in DMSO interacted with lead ion through charge-charge interaction. This PbI_2 -DMSO complex made poor coating, because it could form not hPI structure but PbI_2 complex due to this side reaction. As a result, we chose two solvents: DMF and γ -butyrolactone.

From SEM images in figure 3.12, we figured out that both surface morphology and thickness of hPI were different depending on the types of organic solvent as reported.⁹⁶ Surface morphology of DMF solution-based coating was flat, but some wholes were generated when the solvent evaporated. The averaged thickness of DMF coating was 175.2 nm. On the other hand, surface morphology of γ -butyrolactone solution-based coating was compact film without wholes. The size of aggregated grains was less than 100 nm, and averaged thickness was 181.3 nm.

The reason of these differences between two organic solvents stemmed from three reasons: (1) Viscosity of solvent was different, so it could affect coating homogeneity and uniformity during the spin-coating. (2) Vapor pressure of DMF (b.p. = 152 °C) is higher than γ -butyrolactone, (b.p. = 204 °C) so that DMF evaporation is much easier than γ -butyrolactone. The hPI precipitation started when the solvent dried up. In this step, DMF evaporated faster than γ -butyrolactone to form many nucleation sites. After the nucleation, grain growth determines grain size. If this growth rate is slow, grain will be bigger, vice versa. As DMF evaporation is volatile, the rate of evaporation is rapid and the rate of grain growth should be high without enough time to grow well. In conclusion, because of the fast growth rate, hPI grains with DMF solvent will be smaller than that of γ -butyrolactone. Through SEM images, we confirmed this result by size of grains. (3) Solubility parameter of hPI in each solution was different. This parameter is related with the interaction between solute and solvent. If the interaction is bigger, the solubility parameter will be also bigger. Additionally, there should be strong attractive interaction. As a

result, the rate of OIPs precipitation should be slow in solvent with high solubility parameter to form large grain size. Based on these phenomena, it was predicted that the hPI solubility parameter in γ -butyrolactone is bigger than DMF. In other word, the interaction of hPI is large in γ -butyrolactone compared to DMF. We also checked the same result from SEM images.

3.2.1.3 Pre-treatment dependence

According to previous study, pre-treatment helps to coat well on certain substrates. In this research, we adopted two pre-treatment methods: plasma treatment and preheating. Plasma treatment is widely used method to improve the interface.⁹⁷ Generated plasma attacked the substrate to attach chemical bonds including oxygen-rich functional groups such as hydroxyl and carboxyl group. These oxygen-containing groups are hydrophilic and negatively charged, so that coating behaviors are changed. In comparison, the preheating affects to evaporation of solvent during spin-coating. As we discussed in chapter 3.2.1.2, fast evaporation drives to small size of grain. Important point is that we should set temperature under the boiling point of each solvent.

By analyzing the surface morphology of hPI on Si, (Figure 3.12) both plasma treatment and preheating allow to coat well with high homogeneity. There were no islands and stacked grains compared to non-treated samples. However, preheating had a challenge that the temperature might generate negative damage to substrates such as failure or coating fracture. Additionally, we should take the annealing temperature into consideration when we

fabricate solid-state DSSCs. For example, the optimized annealing temperature of HTM coating was under 60°C. Consequently, it was hard to coat hPI using preheating method in DSSCs fabrication. Comparably, plasma treatment could be applied to make better coating for solid-state solar cells without high annealing temperature.

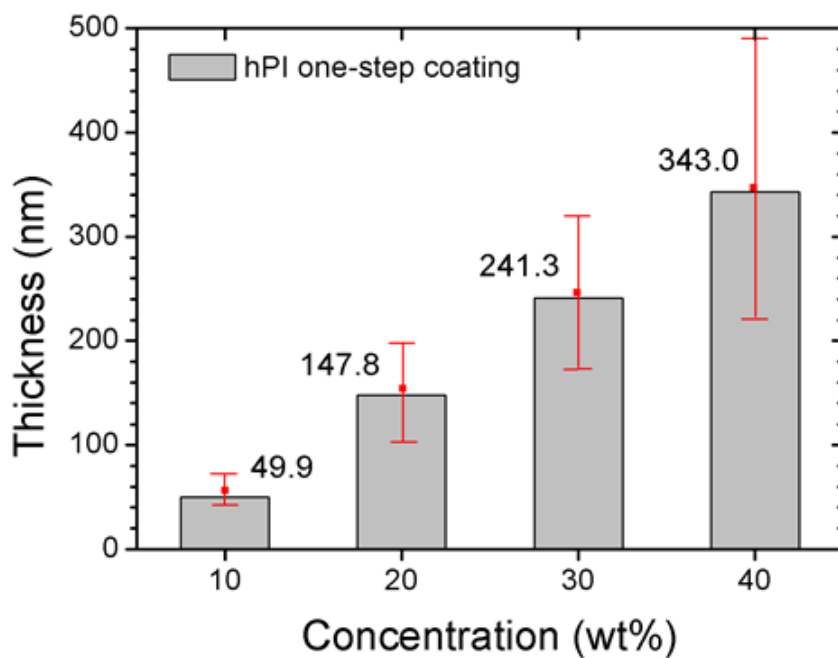


Figure 3.11 hPI thickness variations depending on the concentration. The higher concentration, the thicker film was formed. Less than five different data were calculated and averaged statistically.

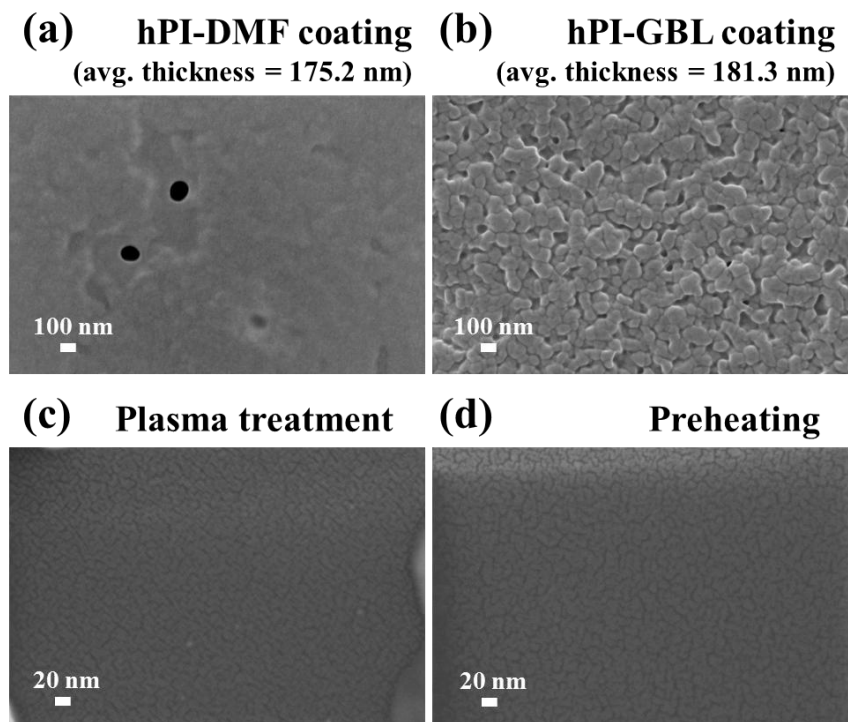


Figure 3.12 SEM images of one-step spin-coated hPI film depending on types of organic solvent and pre-treatments. (a) is DMF solution-based coating, and (b) is γ -butyrolactone solution-based coating. Coating behavior was different: The thickness and grain size of (b) is larger than that of (a). (c) shows plasma-treated coating, and (d) shows preheated coating at 100°C. Through the pretreatment, homogeneous coating was formed.

3.2.2 Two-step coating

Because HPI one-step coating was failed, we focused on different coating method on FTO glass: two-step dip-coating. Not only for HPI, two-step coating (or sequential coating) was confirmed as a way to improve the MPI-based solar cell efficiency by Gratzel's group.⁹⁸ As we explained in chapter 2.2.2.2, the first step is PbI_2 coating, and the next step is dipping the PbI_2 substrate into the organic precursor solution. In this chapter, we optimized several conditions to improve the HPI, hPI coating quality by examining film XRD patterns of perovskites. By this method, we could get optimized two-step conditions for our system.

3.2.2.1 PbI_2 coating dependence

The first step of two-step coating was PbI_2 coating. For homogeneous coating, we treated plasma on FTO substrate. Although PbI_2 is soluble in DMF and DMSO, DMF solvent is better for coating because of DMSO- PbI_2 complex.

The maximum solubility of PbI_2 in DMF is 0.7 M at room temperature, so we set the concentration variables as 0.1 M, 0.3 M, 0.5 M and 0.7 M coating with 2000 rpm 40 sec.⁹⁹ From 0.1 M to 0.7 M, film thickness was confirmed as 51.6 nm ~ 205.6 nm by SEM section images. We statistically analyzed data by averaging less than five thickness values. From 0.5 M, coating thickness was saturated in a range of error bars. It means that PbI_2 coating of

is approximately same in higher concentration than 0.5 M.

Two-step coating let us fabricate homogeneous HPI and hPI coating from organic precursor solution. The solvent was methanol and its concentration was 30 mM. After 5 min of dipping, we could observe the color change caused by perovskites coating. Through film XRD analysis, we figured out that HPI could be grown on the substrate from 0.1 M to 0.7 M. Intensity of characteristic peaks was proportional to PbI_2 concentration. In fact, amounts of HPI coating increased depending on amounts of PbI_2 . Similarly, intensity of hPI characteristic peaks also increased. Interestingly, hPI peaks were not detected when PbI_2 concentration was less than 0.3 M. Two possibilities might be suggested. One is hPI was not created because there were only small amounts of PbI_2 . The other is created hPI was dissolved again into the methanol solvent.

By comparing XRD pattern relying on PbI_2 concentration, we could prove one lesson that high concentration of PbI_2 is beneficial to form large amounts of perovskites coating. For this reason, we used 0.7 M of PbI_2 in following two-step coating. All information related with PbI_2 concentration were summarized in figure 3.13.

3.2.2.2 Concentration of imidazolium iodide dependence

Before identifying the dependence on imidazolium iodide concentration, we chose appropriate solvent to dissolve histidine iodide and histamine iodide. The good solvent for two-step coating should dissolve the salt except

PbI₂. Most in case, alcohols are well-matched solvent in this condition. As a result, we focused on methanol, ethanol and 2-propanol. Histidine iodide/Histamine iodide organic precursor was checked its solubility in each solvent. Both iodides were well dissolved in methanol, but only few amounts of salt were dissolved in 2-propanol. In methanol, the maximum solubility of histidine iodide was 50 mM, while that of histamine iodide was infinite. Based on these preliminary tests, we set the concentration variables as 10 mM, 30 mM and 50 mM because of the solubility limit.

Interestingly, HPI and hPI exhibited similar results. XRD spectra showed that there were few amounts of perovskites in 10 mM organic solution. On the other hand, characteristic peaks of each perovskites increased in 30 mM of solution. It means the coating was created. However, 50 mM of organic solution made the coating collapsed. The intensity of characteristic peaks dramatically decreased, and peaks from organic salts generated its intensity. In other words, the quality of coating got lowered when the concentration of organic solution was very high, and unreacted imidazolium molecules were aggregated on the substrate.

In conclusion, high concentration of organic precursors was not helpful to make perovskites coating. It makes the coating even worse. The appropriate concentration was 30 mM for high quality of coating. With optimized 30 mM of organic solution, we used the same condition in following experiments. Summarized XRD data were plotted in figure 3.14.

3.2.2.3 Dipping time dependence

After the concentration optimization of PbI_2 and organic precursor, we finally focused on the dipping time. With 0.7 M of PbI_2 -DMF solution and 30 mM of imidazolium iodide precursor-methanol solution, we firstly coated perovskites on substrate, and then measured XRD pattern.

In the case of HPI, two characteristic peaks located at 22.5° and 28.5° maximized at 5 min. Before 5 min, the coating was not fully developed. Especially for 1 min, PbI_2 did not completely react and even it was detected by XRD. It means that reaction kinetics or crystallization rate requires at least 1 min for two-step coating. After 5 min, the intensity of HPI peaks gradually decreased. By this phenomenon, we confirmed that long dipping time could not make beneficial effects to two-step coating.

Comparably, hPI showed different results. The characteristic peak of hPI located at 28.0° was increased from 1 min to 7 min, and maximized. In other words, hPI two-step coating was well-developed at 7 min of dipping. Nevertheless, in the case of 9 min, the characteristic peak totally collapsed to zero. It was dramatical change. The possible reason is that created hPI film was dissolved into methanol solvent because PbI_2 was not detected by XRD analysis: hPI degradation cannot be the reason. Through the optimization of dipping time, we concluded that 5 min of dipping is the best condition for HPI two-step coating, and 7 min of dipping is the best for hPI coating. (Figure 3.15)

It was the first time to discover the coating behavior of HPI and hPI.

Optimized conditions including concentration and time were worth noting to improve the interface for high efficient solid-state solar cells.

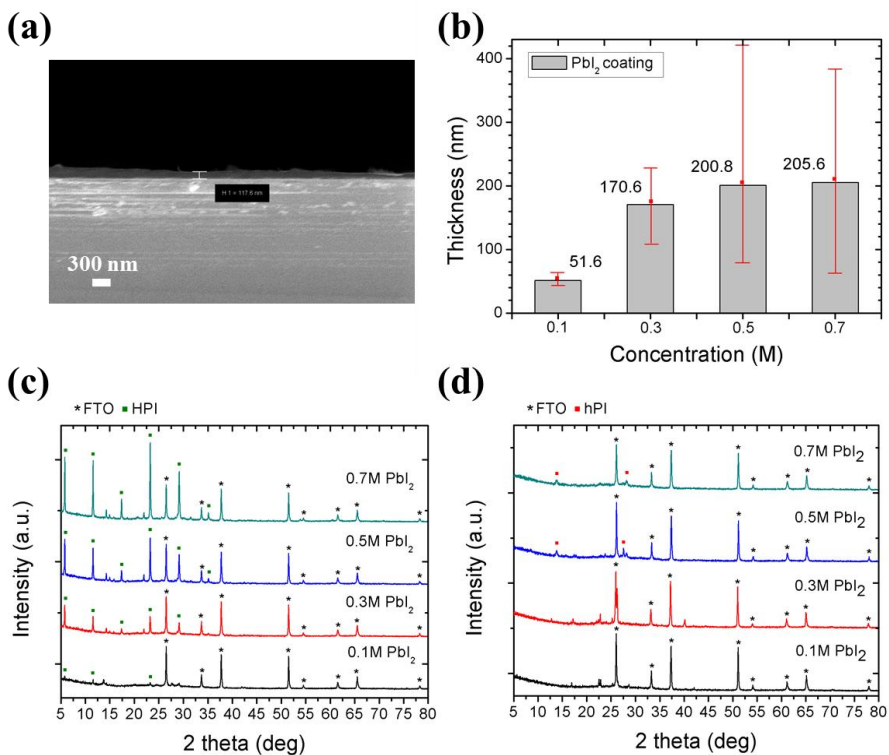


Figure 3.13 (a) Section SEM image of uniform PbI_2 coating, (b) dependence of thickness on PbI_2 concentration, two-step coated (c) HPI and (d) hPI film XRD data depending on PbI_2 concentration. Peak intensity of HPI and hPI was proportional to PbI_2 concentration. However, hPI crystals were not created under the 0.3M of PbI_2 .

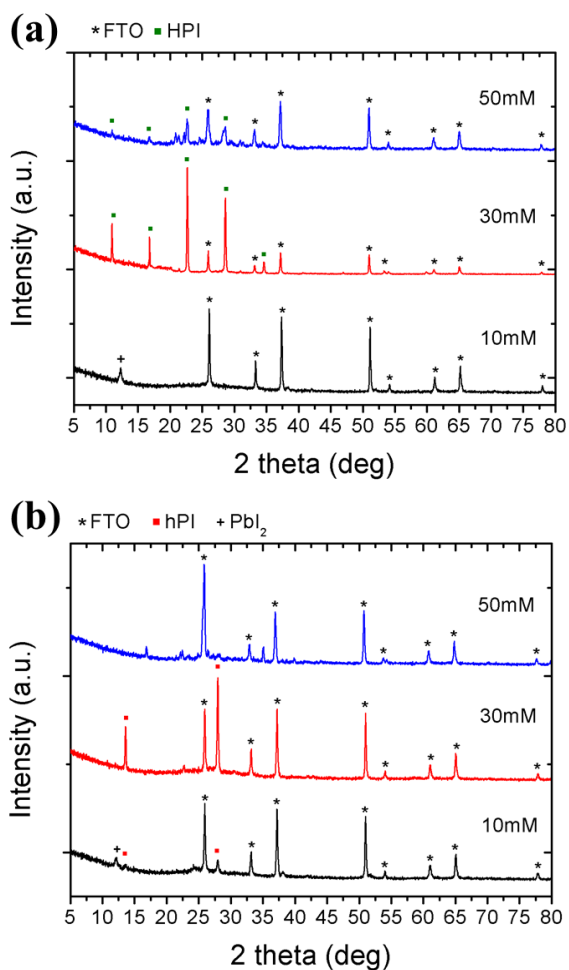


Figure 3.14 Two-step (a) HPI and (b) hPI film XRD data depending on the concentration of imidazolium iodide from 10 mM to 50 mM. Solvent was methanol. At 30mM, both HPI and hPI showed maximum intensities. At higher concentration, organic salts were left on the substrate. On the other hand, there were only few HPI, hPI at lower concentration.

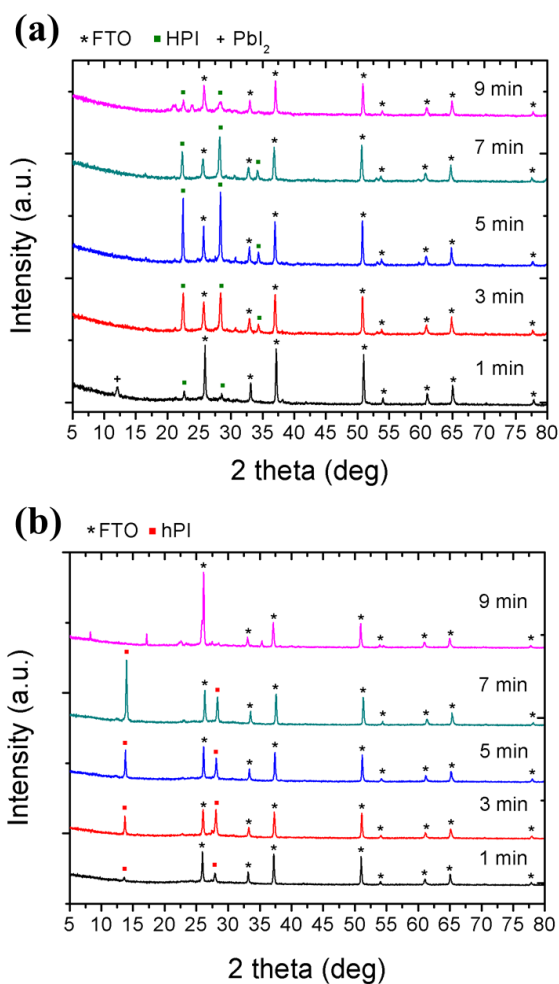


Figure 3.15 Two-step (a) HPI and (b) hPI film XRD data depending on dipping time. In figure (a), the HPI characteristic peaks were maximized at 5 min of dipping, and slowly degraded after 5 min. On the other hand, in figure (b), the characteristic peaks of hPI were maximized at 7 min of dipping, and totally collapsed at 9 min.

3.3 Photovoltaic characterization

3.3.1 Photoactivity determination and screening

Before the solar cell fabrication, our new synthesized OIPs should be examined if they have photoactivity or not.¹⁰⁰ The reason was that fabrication methods for solid-state solar cells were intricate and costly. In fact, the photocurrent measurement was needed to reduce unnecessary trials, and to check the potential as photosensitizer preliminarily. Photoactivity screening was simply measured by two-point probe station under light source. As we introduced in 2.3.5, our synthesized HPI or hPI was coated on FTO glass, and gold was thermally evaporated to make electrodes. For reducing contact error and leakage current between the substrate and electrode, we treated TiO₂ first for blocking film.

Primarily, HPI was measured through our screening. Unfortunately, HPI showed very high resistance around few GΩ. Poor conductivity was also detected not only by measuring resistivity, but also by charging phenomena in SEM images. Because of not uniformed coating and high conductivity, photocurrent from HPI perovskite was hard to be observed. On the other hand, hPI perovskites showed clear photoactivity whose photocurrent was about 20 nA at 1 μV. During light holding 120 sec under 300 W of Xe lamp, the hole-electron pairs were generated in hPI. After that, generated photo-induced electrons moved to electrode to flow the current. In figure 3.16, we figured out that the sequence of light blinking allowed photocurrent also be blinking

at the same time per each 60 sec.

It was our new approach to get the clue of photoactivity in a simple and easy way. Through the photocurrent measurement, we confirmed that hPI has the activity under the sunlight, and has the potential to be utilized as photosensitizer in solid-state solar cells. Our screening method was helpful not only for searching the photoactive OIPs, but also for testing dependence of conductivity shift preliminarily.

3.3.2 Band analysis for solid-state solar cells

Band analysis also helps us to predict the performance of photosensitizer before we use. The maximum open circuit voltage should be 1.22 V, because this value is the gap between TiO_2 conduction band and redox potential of spiro-MeOTAD. Additionally, we can predict certain sensitizer is able to work as sensitizing materials or not. In this chapter, we discussed the possibility of photosensitizer in solid-state perovskite cells with our new imidazole-based OIPs.

Significantly, two conditions must be satisfied for photosensitizer in our TiO_2 and spiro-MeOTAD system. The first one is that conduction band OIPs should be higher than that of TiO_2 . Light induced electrons should be generated from OIPs and go into TiO_2 to make the electron flow. If conduction band is not matched, these photo-electrons cannot pass through TiO_2 layer.

The second condition is that valence band of OIPs should be lower than redox potential of spiro-MeOTAD. Spiro-MeOTAD is a hole-transfer material. It means holes separated by solar power should transfer from OIPs to spiro-MeOTAD. Similar to the example of conduction band, if band position is not matched, the flow of hole will be stopped. In other words, mismatched OIPs could not be used as photosensitizer. Additionally, for high efficient solar cells, sensitizing material should absorb a lot of light.

In figure 3.17, we summarized the structure of solid-state perovskite solar cell. Based on two conditions above, only MPI and hPI could be the photosensitizing materials. HPI could not work, because the conduction band of HPI is lower than that of TiO₂. Unfortunately, the band gap energy of hPI (2.23 eV) is larger than that of MPI (1.5 eV), so that previous MPI has more advantage to collect the visible light including red region. However, hPI also could be utilized as color-tuned photosensitizer. Consequently, in this chapter, we got scientific clue that hPI-sensitizing solid-state cell could work well.

3.3.3 I-V spectra analysis

Based on the previous discussion, we chose hPI photosensitizer. In this chapter, we fabricated hPI-based solid-state perovskite cells using one-step spin-coating and two-step dip-coating. Through the results in chapter 3.2, initiative conditions of cells were equally set. The reason was that optimized coating conditions might directly connect to conditions of maximum cell

performance. However, the difference could be generated. For example, substrates were not same; FTO glass in chapter 3.2, while mp-TiO₂ layer in solar cells. Additionally, pore-filling, sensitizer absorbance, size of grains could be changed.¹⁰¹ Therefore, many variables were needed to optimize again for high efficient perovskite cells. We considered possible deviation from initiative conditions during the measurement.

After the fabrication, we measured the cell performance by solar simulator. The active area was 1.4 cm² under the one sun and 100mW/cm². As we deposited four electrodes on each cell, it was necessary to pick up the maximum electrode from one of them. By comparing maximum current density and voltage, we chose one datum which has the highest power. After then, fill factor and efficiency were calculated.

3.3.3.1 One-step coated cells optimization

For one-step hPI cells, we set four variables: pretreatment, annealing temperature, concentration and thickness of TiO₂. For comparison, we also set the reference cell with no plasma treated, 100 °C annealing, 20 wt% γ -butyrolactone solution, 500 nm of TiO₂. The color of one-step hPI cell was light orange with uniformity.

The pretreatment caused positive effects on cell parameters. Compared to reference cell, generated J_{SC} was much higher. Because J_{SC} is a factor of diffusion, it could be recognized that the diffusion was not good in reference

cell. From SEM images in figure 3.12, the uniform coating of perovskites let electrons and holes move to electrodes quickly. Surface morphology of non-treated coating was too ragged to conduct electron/hole freely. Measured J_{SC} and efficiency was almost half of those of treated cells. For this reason, we concluded that the pretreatment is needed to improve the cell performance.

The second variable was annealing temperature. From 50 °C to 100 °C, the cell performance was increased. However, above 150 °C, efficiency started to degrade to 21%. Therefore, we chose 100 °C annealing as an optimum.

Concentration dependence was easy to be recognized. 5 wt% of hPI solution showed both lowest J_{SC} and V_{OC} . The higher concentration, the more hPI perovskites were in γ -butyrolactone. In fact, the concentration dependence was stemmed from amounts of hPI on TiO_2 substrate. However, at 30 wt% of solution, cell performance decreased. Because the maximum hPI solubility is around 30 wt%, some hPI crystals already precipitated at higher concentration. This non-homogeneous oversaturation occurred poor coating. This result is similar with previous researches on MPI: the coating with saturated solution showed the best performance.

Dependence on TiO_2 thickness gave us a lot of lessons. Thick TiO_2 layer can absorb more perovskites. Therefore, it was expected that 1000 nm of TiO_2 showed higher efficiency than 300 nm TiO_2 . However, result was totally different: 300 nm of TiO_2 exhibited the highest performance. The result indicated two facts. (1) hPI has many recombination sites to lose generated electron-hole pairs, so that generated exciton cannot go through the thick TiO_2 layer. Because the lifetime of exciton of 2-dimensional

perovskites is relatively short, (high exciton binding energy) photo-induced electrons are easy to turn back to neutral state. (2) hPI has low absorption coefficient. If the coefficient is bigger enough to absorb light, heavily loaded 1000 nm of cell should have generated high activity. However, it was not. To sum up, the key factor of hPI light absorbing activity was not dependent on the amount, but dependent on the lifetime of exciton.

From these results, optimized conditions for one-step hPI cells were 300nm of mp-TiO₂, 100 °C annealing, and 30wt% of solution with plasma treatment.

3.3.3.2 Two-step coated cells optimization

We fabricated two-step cells by using organic salt solution in methanol. The reference cell was fabricated with 500 nm of TiO₂, 30 mM, 5 min of dipping that are same with optimized condition in chapter 3.2. Additionally, annealing temperature, TiO₂ thickness, concentration of imidazolium salt solution was checked to optimize the performance.

Unfortunately, the properties of solar cells were worse than one-step coating. (Figure 3.19) Except few cells, J_{SC} was measured in a range of error current. These noise currents are also generated in simple contact between TiO₂ and spiro-MeOTAD. In fact, two-step cell performance was hard to compare with ordinary cells. Predicted reasons for failure of two-step coated hPI cells might be caused by (1) crystallization kinetics, (2) temperature

change during the coating, (3) organic iodide salts remaining on hPI, and (4) dissolution of hPI in methanol. Among four factors, crystallization kinetics took major role of failure. In the case of MPI, the rate of crystallization is high enough to make many nucleation sites at once.^{102, 103} However, kinetics of hPI is slow: only small sites of nucleation started to grow to make large crystals on mp-TiO₂ layer. Because of the large grain size, hPI could not fully penetrate into the pore.

Additionally, temperature was changed during two-step dipping. This may cause not uniform coating. Moreover, after the organic solution evaporation, some histamine iodide salts were remained on the substrate. It generated negative effects on interface or contact between perovskites and spiro-MeOTAD. In other word, it disturbed the hole transfer. Long-time dipping also caused poor coating behavior, because crystallized hPI could be dissolved in methanol.

Consequently, two-step fabrication was not appropriate method for hPI. In MPI, it works very well due to its fast nucleation to form small grain sizes. On the other hand, hPI in our system has slow grain growth rate to make big crystals during two-step dipping.

3.3.3.3 Long term stability test

After the cell fabrication, the stability should be guaranteed for commercial application. In the case of MPI cell, perovskites decomposed only after 6 hours. For this reason, water-resistant OIPs should be prepared

for photosensitizer.

For verifying the preliminary long term stability, we prepared OIPs coating on FTO glass. Through XRD pattern, we confirmed that hPI structure was stable during long range of time. By the peak ratio between hPI characteristic peak and FTO reference peak, only 36.7% of hPI decomposed after 10 days. (Figure 3.20) It was highly stable compared to MPI without any protection. In the same atmosphere, MPI decomposed to PbI_2 completely only after 6 hours.

Long term stability of cell performance also should be checked. For 120 hours, we measured sequential I-V data with the same reference cell. After 5 days later, the cell parameters decreased: 21.9% of J_{SC} , 1.21% of V_{OC} , 12.9% of fill factor, and 38.5% of efficiency. As hPI was protected in fabricated solar cells by spiro-MeOTAD or electrode, the degradation was slowly processed than simple FTO coating. On the other hand, MPI cell with dark brown color was totally gone only after 40 hours. Through the long term stability test, we examined that hPI could survive about 1.5~2 times longer than MPI under the normal atmosphere.

The reason of high stability of hPI can be analyzed by the halogen bonding that we mentioned in chapter 3.1.1. The reason of OIPs degradation is humidity. Water molecules can intervene to the organic-inorganic binding sites to break bonds. In this case, imidazole ring makes stronger interaction than primary ring, so that there is less potential for water to get into the lattice. Consequently, degradation of hPI can be slow compared to that of MPI.

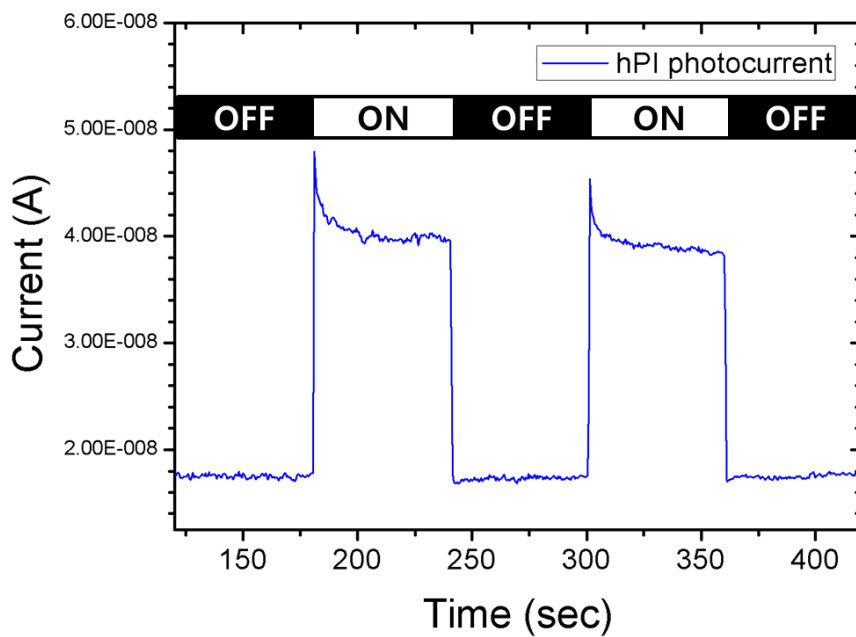


Figure 3.16 Photocurrent generation from hPI perovskite at 0.001 V, 2 min of holding. We used two-point probe station for materials screening. Depending on the existence of light, 20 nA of photocurrent was generated.

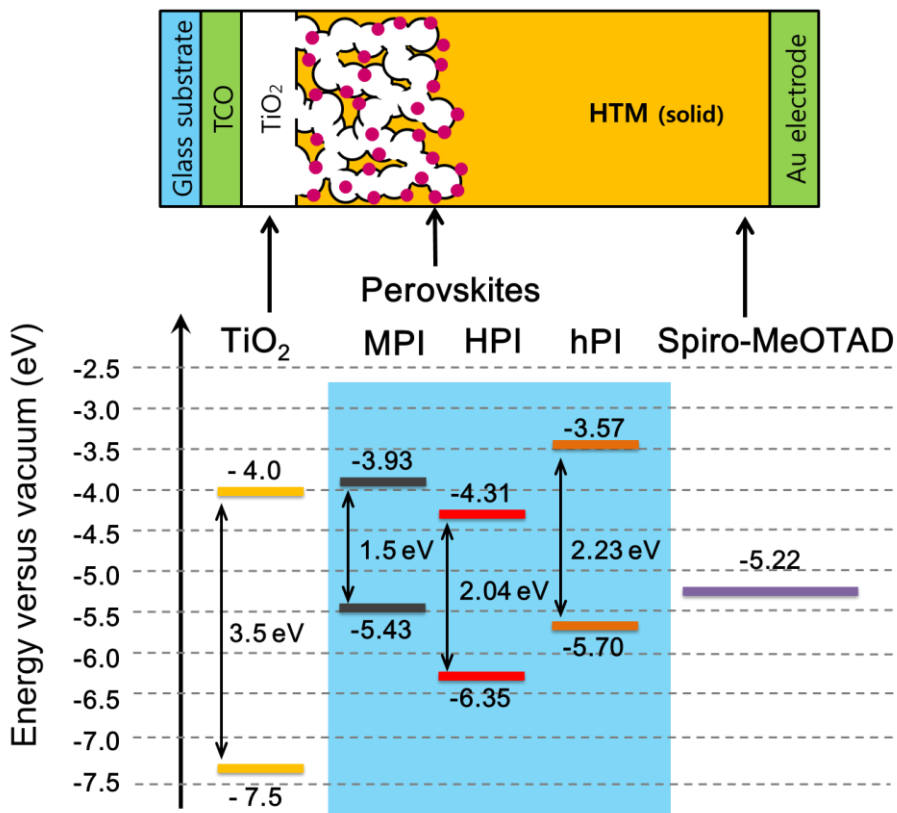


Figure 3.17 Schematic band alignment for solid-state solar cells with structure. Band position of MPI, HPI, and hPI is sketched in the middle of the figure. Conduction band of TiO₂ should be lower than conduction band of perovskites to collect photo-induced electrons. On the other hand, redox potential of spiro-MeOTAD should be higher than valence band of perovskites to conduct holes. Based on the band structure, MPI and hPI are suitable to be utilized as photosensitizer.

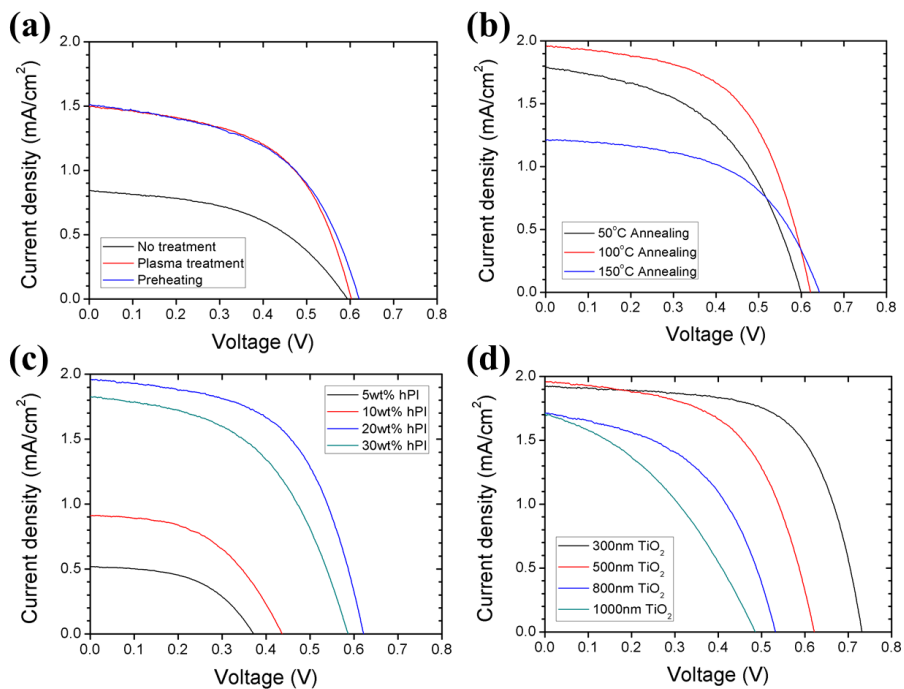


Figure 3.18 Optimization of one-step hPI cells based on I-V analysis. (a) Pretreatment dependence: Pretreatment helped to increase the cell efficiency (b) Annealing temperature dependence: 100 °C annealing showed maximum efficiency (c) Concentration dependence: Cell performance was increasing until 20wt%. At 30wt%, the efficiency got lowered because of unstable hPI solution. (d) mp-TiO₂ thickness dependence: the thinner TiO₂ generated the higher efficiency. Cell parameters are summarized in Table 3.

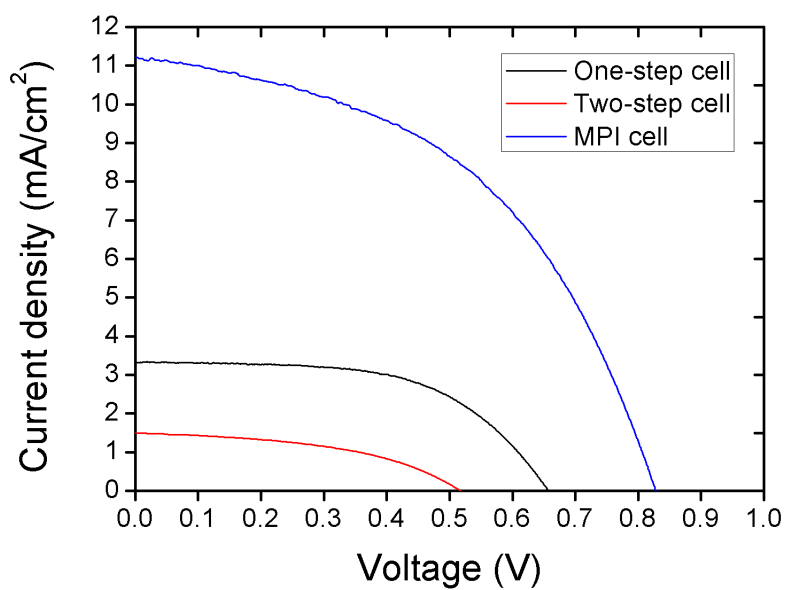


Figure 3.19 Efficiency comparisons among one-step hPI cell, two-step hPI cell, and MPI cell. Performance of one-step hPI cell was better than that of two-step cell. The maximum efficiency of hPI cell was 1.26%, while efficiency of MPI cell was 4.19 %.

Table 3. Photovoltaic parameters of one-step hPI solid-state solar cells

	J_{sc} (mA/cm²)	V_{oc} (V)	Fill factor	Efficiency (%)
Reference				
20 wt%, 100 °C, 500 nm TiO ₂	1.96	0.72	0.488	0.69
No treatment	0.85	0.59	0.489	0.24
Plasma	1.50	0.60	0.547	0.49
Preheating	1.51	0.62	0.519	0.49
50 °C	1.79	0.60	0.494	0.53
150 °C	1.21	0.64	0.544	0.42
5 wt%	0.52	0.37	0.514	0.10
10 wt%	0.91	0.44	0.494	0.20
30 wt%	1.83	0.59	0.500	0.54
300nm TiO ₂	1.92	0.73	0.654	0.92
800nm TiO ₂	1.71	0.63	0.417	0.45
1000nm TiO ₂	1.71	0.59	0.310	0.31

Table 4. Photovoltaic parameters of two-step hPI solid-state solar cells

	J_{sc} (mA/cm²)	V_{oc} (V)	Fill factor	Efficiency (%)
Reference				
30mM, 100°C, 500 nm TiO ₂	0.33	0.56	0.340	0.062
10mM	1.50	0.52	0.459	0.358
50mM	0.84	0.43	0.332	0.120
50°C	0.24	0.49	0.525	0.062
150°C	0.12	0.51	0.480	0.031
300nm TiO ₂	0.07	0.08	0.328	0.002
800nm TiO ₂	0.33	0.43	0.458	0.017
1000nm TiO ₂	0.08	0.43	0.378	0.028

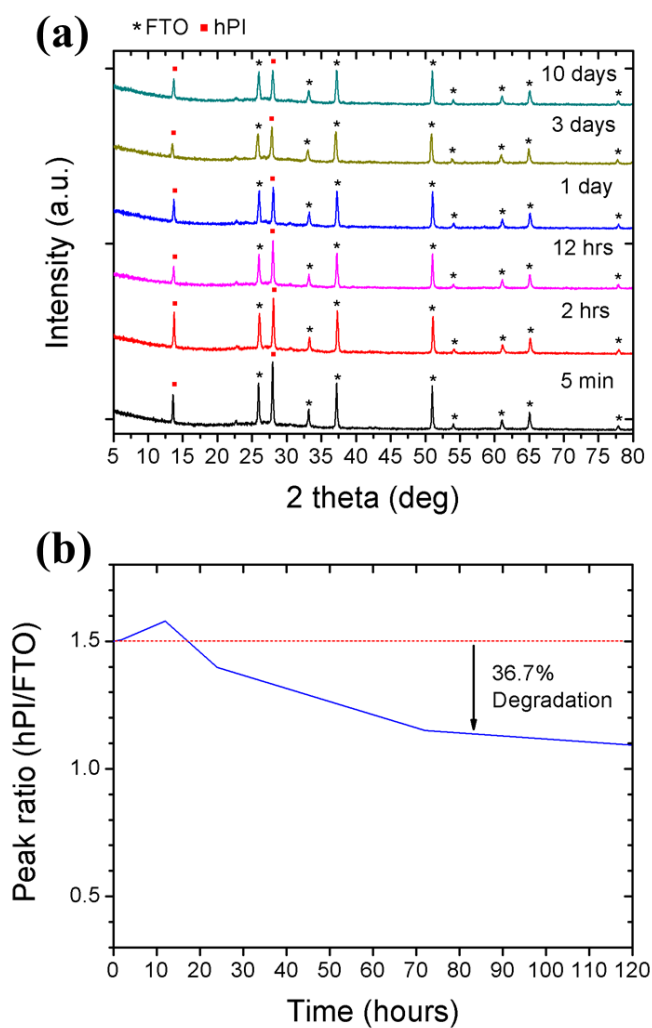
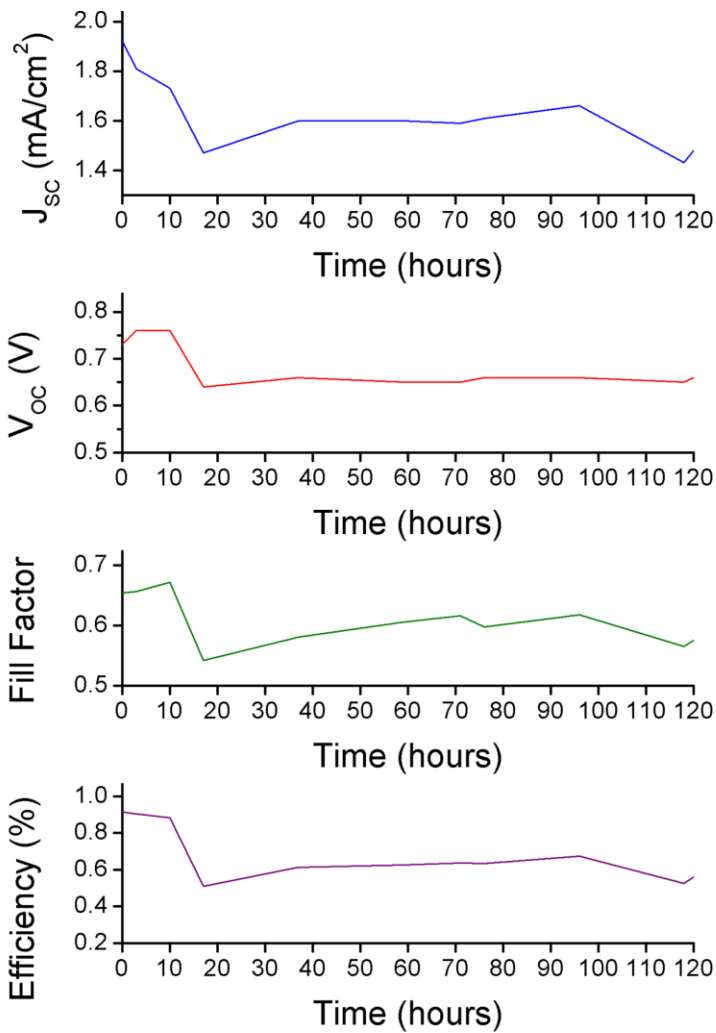


Figure 3.20 Long term stability of hPI perovskite coating on FTO glass. (a) It was noticeable that hPI structure had maintained for 10 days: characteristic peaks did not collapse. (b) By comparing hPI and FTO peak intensities, we confirmed that only 36.7% of hPI decomposed after 10 days without any protection.



	J_{sc}	V_{oc}	Fill factor	Efficiency
Degradation After 120 hours	21.9 %	12.1 %	12.9 %	38.5 %

Figure 3.21 Cell stability plots of hPI perovskite cells by comparing J_{sc} , V_{oc} , fill factor and efficiency for 120 hours. Degradation ratio of each parameter is summarized in the table.

Chapter 4. Conclusion

In this research, we synthesized solution-based new imidazole-based organic-inorganic perovskites. Compared to the previously reported methyl ammonium lead iodide, we successfully changed the color and band gap by using different organic molecules. Imidazole-involved biomolecules, histidine and histamine were used as organic chains in OIPs. To synthesize the organic salt, we used acid-base reaction between histidine/histamine and hydriodic acid. After that, the perovskites were synthesized with PbI_2 in an organic solvent at 60°C .

For the determination of the crystal structure, we conducted preliminary investigation using SEM images and powder XRD pattern. HPI had a diamond shape whose characteristic peaks were located at 22.5° and 28.5° . On the other hand, hPI had a rectangular shape whose characteristic peak was located at 28.0° . To verify the exact crystal structure, we analyzed a single crystal by synchrotron. The obtained crystal was monoclinic, and its symmetry was $P2_1/c$. We found out that halogen bonds are formed not only by primary amine, but also by the whole imidazole ring interacting with inorganic octahedrons. It was possible to recognize that the imidazole ring could be the plugging-in group with large binding energy.

The color of synthesized salt was dark red (HPI) and orange (hPI). By measuring the reflectance and absorbance spectra, we showed that these two OIPs were interacting with visible light. For the calculation of band gap energy, we transformed reflectance to Kubelka-Munk diagram. Calculated

band gap energy was 2.04 eV for HPI, and 2.23 eV for hPI, respectively. Additionally, we also figured out the valence band position by UPS. The valence band of HPI was at -6.35 eV, and hPI was at -5.70 eV. Through the band structure analysis, we confirmed that hPI could be utilized as photosensitizer in solid-state solar cells. To add, we confirmed that our OIPs could survive at 260 °C (HPI) and 310 °C (hPI) by TGA analysis.

After the analysis on materials' properties, we checked the coating behaviors of each OIPs. One-step spin-coating was conducted only for hPI, because of the irregular coating of HPI. Pretreatments including plasma treatment and preheating led hPI to coat well on the substrate. Types of organic solvents also caused the different morphology of hPI. After that, we used two-step dip-coating to coat not only hPI, but also HPI uniformly. Through the XRD analysis, hPI was well coated at 0.7 M of PbI_2 and 7 min of dipping with 30mM of organic precursor methanol solution. In the case of HPI, 0.7 M of PbI_2 , 5 min of dipping with 30 mM of organic solution was the optimized conditions.

hPI-based solid-state solar cells were fabricated using both coating techniques. For the one-step cell, the performance was dependent on variables including pretreatment, annealing temperature, concentration, and TiO_2 thickness. The optimized conditions for one-step cell was 100 °C annealing temperature, 20 wt%, 300 nm of TiO_2 with pretreatment. On the other hand, the two-step cell did not perform high activity as the one-step cell, because of the recrystallization rate and pore filling. Compared to the MPI cell, the hPI cell was much more stable in a humid atmosphere as proven by long term

stability test. After 120 hours, hPI performance degraded by only about 38.5 %, while MPI performance almost disappeared. We analyzed the reason for this phenomena lied in the organic-inorganic interaction in crystal lattice.

In conclusion, we discovered new imidazole-based OIPs using biomolecules, and characterized their various properties. In addition, by coating behavior analysis and I-V plot analysis, we fabricated a maximum 1.26 % of hPI-based perovskites cell which proved to be more stable than the previous MPI cell.

References

1. Z. Cheng, et al., Layered organic-inorganic hybrid perovskites: structure, optical properties, film preparation, patterning and templating engineering, *CrystEngComm.*, **12**, (2010) 2646-2662.
2. A. M. Belcher, et al., Control of crystal phase switching and orientation by soluble mollusc-shell proteins, *Nature*, **381**, (1996), 56-58.
3. D. Guerin, Synthesis and electrical properties of fullerene-based molecular junctions on silicon substrate, *J. Mater. Chem.*, **20**, (2010), 2680-2690.
4. H. Li, et al., Design and synthesis of an exceptionally stable and highly porous metal-organic framework, *Nature*, **402**, (1999), 276-279.
5. R. Deena, et al., Solvothermal synthesis of perovskites and pyrochlores: crystallisation of functional oxides under mild conditions, *Chem. Soc. Rev.*, **39**, (2010) 4303-4325.
6. S. B. Ott, *Crystallography: An introduction*, 3rd ed., Springer (2012)
7. Y. Lu, et al., Effect of strain and tetragonal lattice distortions in doped perovskite manganites, *Phys. Rev. B.*, **73**, (2006) 184406.
8. M. Johansson, et al., Perovskites and thin films- crystallography and chemistry, *J. Phys.: Cond. Matter*, **20**, (2008) 264001.
9. P. G. Romero, et al, *Functional hybrid materials*, 6th ed., Wiley, (2004)
10. J. H. Rhee, et al., A perspective of mesoscopic solar cells based on metal chalcogenide quantum dots and organometal-halide perovskites, *NPG Asia Materials*, **5**, (2013)
11. J. N. Israelachvili, *Intermolecular and Surface Forces*, 3rd ed. (2011)
12. D. B. Mitzi, et al., Synthesis, resistivity, and thermal properties of the

- cubic perovskite $\text{NH}_2\text{CH}=\text{NH}_2\text{SnI}_3$ and related systems, *J. Solid State Chem.*, **134**, (1997) 376-381.
13. D. B. Mitzi, et al., Organic-inorganic electronics, *IBM J. Res. & Dev.*, **45**, (2001) 29-45.
14. D. B. Mitzi, et al., Conducting layered organic-inorganic halides containing <110>-oriented perovskite sheets, *Science*, **267**, (1995) 1473-1476.
15. J. Zaleski, et al., Structure at 200 and 298 K and X-ray investigations of the phase transition at 242 K of $[\text{NH}_2(\text{CH}_3)_2]_3\text{Sb}_2\text{Cl}_9$ (DMACA), *Acta Crystallogr., Sect. B: Struct. Sci.*, **52**, (1996) 287-295.
16. D. B. Mitzi, Solution-processed inorganic semiconductors, *J. Mater. Chem.*, **14**, (2004) 2355-2365.
17. D. B. Mitzi, Synthesis, structure and properties of organic-inorganic perovskites and related materials, *Prog. Inorg. Chem.*, **48**, (1999) 1-121.
18. X. Huang, et al., Flexible hybrid semiconductors with low thermal conductivity: The role of organic diamines, *Angew. Chem. Int. Ed.*, **48**, (2009) 7871-7874.
19. L. Xue, et al., Dewetting behavior of polystyrene film filled with $(\text{C}_6\text{H}_5\text{C}_2\text{H}_4\text{NH}_3)_2\text{PbI}_4$, *J. Chem. Phys.*, **129**, (2008) 054905.
20. D.B. Mitzi, Templating and structural engineering in organic-inorganic perovskites, *J. Chem. Soc., Dalton Trans.*, (2001) 1-12.
21. M. Braun, et al., Tailoring of energy levels in lead chloride based layered perovskites and energy transfer between the organic and inorganic planes, *Chem. Phys. Lett.*, **303**, (1999) 157-164.
22. C. Constantinou, et al, Semiconducting tin and lead iodide perovskites with organic cations: Phsed transitions, high mobilities, and near-infrared photoluminescent properties, *Inorg. Chem.*, **52**, (2013) 9019-9038.

23. D. B. Mitzi, Organic-inorganic perovskites containing trivalent metal halide layers: the templating influence of the organic cation layer, *Inorg. Chem.*, **39**, (2000) 6107-6113.
24. D. B. Mitzi, et al., Conducting tin halides with a layered organic-based perovskites structure, *Nature*, **369**, (1994) 467-469.
25. C. R. Kagan, et al., Organic-inorganic hybrid materials as semiconducting channels in thin-film field-effect transistors, *Science*, **286**, (1999) 945-947.
26. D. B. Mitzi, et al., Design, structure, and optical properties of organic-inorganic perovskites containing an oligothiophene chromophore, *Inorg. Chem.*, **38**, (1999) 6246-6256.
27. G. C. Papavassiliou, et al., Some new organic-inorganic hybrid semiconductors based on metal halide units: structural, optical and related properties, *Adv. Mater. Opt. Electron.*, **9**, (1999) 791-800.
28. D. B. Mitzi, et al., Structurally tailored organic-inorganic perovskites: Optical properties and solution-processed channel materials for thin-film transistors, *Chem. Mater.*, **13**, (2001) 3728-3740.
29. K. Chondroudis, et al., Electroluminescence from an organic-inorganic perovskite incorporating a quaterthiophene dye within lead halide perovskite layers, *Chem. Mater.*, **11**, (1999), 3028-3030.
30. N. O. Yamamuro, et al., Dielectric study of $\text{CH}_3\text{NH}_3\text{PbX}_3$ ($\text{X} = \text{Cl}, \text{Br}, \text{I}$), *J. Phys. Chem. Solid*, **53**, (1992) 935-939.
31. A. S. Bhalla, et al., The perovskite structure- a review of its role in ceramic science and technology, *Mater. Res. Innovations*, **4**, (2000) 3-26.
32. C. A. Randall, et al, Classification and consequences of complex lead perovskite ferroelectrics with regard to B-site cation order, *J. Mater. Res.*, **5**, (1990) 829-834.

33. B. O'Regan, et al., A low-cost, high-efficiency solar cell based on dye-sensitized colloidal TiO₂ films, *Nature*, **353**, (1991) 737-740.
34. M. Gratzel, Photoelectrochemical cells, *Nature*, **414**, (2001) 338-344.
35. H. Tributsch, et al., Dye sensitization solar cells: a critical assessment of the learning curve, *Coordination Chem. Rev.*, **248**, (2004) 1511-1530.
36. D. Kuang, et al., High molar extinction coefficient heteroleptic ruthenium complexes for thin film dye-sensitized solar cells, *J. Am. Chem. Soc.*, **128**, (2006) 4146-4154.
37. K. Tennakone, et al., A dye-sensitized nano-porous solid state photovoltaic cell, *Semiconductor Science and Technology*, **10**, (1995) 1689.
38. K. Tsujimoto, et al., TiO₂ surface treatment effects by Mg²⁺, Ba²⁺, and Al³⁺ on Sb₂S₃ extremely thin absorber solar cell, *J. Phys. Chem. C.*, **116**, (2012) 13465-13471
39. Q. B. Meng, et al., Fabrication of an efficient solid-state dye-sensitized solar cell, *Langmuir*, **19**, (2003) 3572-3574.
40. B. O'Regan, et al., A solid-state dye-sensitized solar cell fabricated with pressure-treated P25-TiO₂ and CuSCN: Analysis of pore filling and IV characteristics, *Chem. Mater.*, **14**, (2002) 5023-5029.
41. K. Tennakone, et al., An efficient dye-sensitized photoelectrochemical solar cell made from oxides of tin and zinc, *Chem. Comm.*, (1999) 15-16.
42. M. Wang, et al., Solid-state dye-sensitized solar cells using ordered TiO₂ nanorods on transparent conductive oxide as photoanodes, *J. Phys. Chem. C*, **116**, (2012) 3266-3273.
43. J. Li, et al., Nanocomposites of ferroelectric polymers with TiO₂ nanoparticles exhibiting significantly enhanced electrical energy density, *Adv. Mater.*, **21**, (2009) 217-221.

44. A. Yella, et al., Porphyrin-sensitized solar cells with cobalt (II/III)-based redox electrolyte exceed 12 percent efficiency, *Science*, **334**, (2011) 629-634.
45. I. Chung, et al., All-solid-state dye-sensitized solar cells with high efficiency, *Nature*, **485**, 486-489.
46. D. P. Hagberg, et al., Symmetric and unsymmetric donor functionalization comparing structural and spectral benefits of chromophores for dye-sensitized solar cells, *J. Mater. Chem.*, **19**, (2009) 7232-7238.
47. S. M. Feldt, et al., Design of organic dyes and cobalt polypyridine redox mediators for high-efficiency dye-sensitized solar cells, *J. Am. Chem. Soc.*, **132**, (2010) 16714-16724.
48. S. M. Feldt, et al., Effects of driving forces for recombination and regeneration on the photovoltaic performance of dye-sensitized solar cells using cobalt polypyridine redox couples, *J. Phys. Chem. C*, **115**, (2011) 21500-21507.
49. J. A. Chang, et al., Panchromatic photon-harvesting by hole-conducting materials in inorganic-organic heterojunction sensitized-solar cell through the formation of nanostructured electron channels, *Nano Lett.*, **12**, (2012) 1863-1867.
50. S. H. Im, et al., All solid state multiply layered PbS colloidal quantum-dot-sensitized photovoltaic cells, *Energy Environ. Sci.*, **4**, (2011) 4181-4186.
51. U. B. Cappel, et al., A broadly absorbing perylene dye for solid-state dye-sensitized solar cells, *J. Phys. Chem. C*, **113**, (2009) 14595-14597.
52. A. Hagfeldt, et al., Dye-sensitized solar cells, *Chem. Rev.*, **110**, (2010) 6595-6663.
53. K. Bouzidi, et al., Solar cells parameters evaluation considering the series and shunt resistance, *Solar Energy Materials and Solar Cells*, **91**, (2007)

1647-1651.

54. B. O'Regan, et al., Electrodeposited nanocomposite n-p heterojunctions for solid-state dye-sensitized photovoltaics, *Adv. Mater.*, **12**, (2000) 1263-1267.
55. H-S. Kim, et al., Lead iodide perovskite sensitized all-solid-state submicron thin film mesoscopic solar cell with efficiency exceeding 9%, *Scientific Reports*, **2**, (2012) 591-597.
56. M. M. Lee, et al, Efficient hybrid solar cells based on meso-superstructured organometal halide perovskites, *Science*, **338**, (2012) 643-647.
57. T. Baikie, et al., Synthesis and crystal chemistry of the hybrid perovskite (CH₃NH₃)PbI₃ for solid-state sensitized solar cell applications, *J. Mater. Chem.*, **1**, (2013) 5628.
58. N-G. Park, Organometal perovskite light absorbers toward a 20% efficiency low-cost solid-state mesoscopic solar cell, *J. Phys. Chem. Lett.*, **4**, (2013) 2423-2429.
59. G. Xing, et al., Long-range balanced electron- and hole-transport lengths in organic-inorganic CH₃NH₃PbI₃, *Science*, **342**, (2013) 344-347.
60. J. M. Ball, et al., Low-temperature processed meso-superstructured to thin-film perovskite solar cells, *Energy Environ. Sci.*, **6**, (2013) 1739-1743.
61. A. Kojima, et al., Organometal halide perovskites as visible-light sensitizers for photovoltaic cells, *J. Am. Chem. Soc.*, **131**, (2009) 6050-6051.
62. J. H. Heo, et al., Efficient inorganic-organic hybrid heterojunction solar cells containing perovskite compound and polymeric hole conductors, *Nature Photonics*, **7**, (2013) 486-491.
63. S. Colella, et al., MAPbI_{3-x}Cl_x mixed halide perovskite for hybrid solar cells: The role of chloride as dopant on the transport and structural properties,

- Chem. Mater.*, **25**, (2013) 4613-4618.
64. D. Bi, et al., Using a two-step deposition technique to prepare perovskite ($\text{CH}_3\text{NH}_3\text{PbI}_3$) for thin film solar cells based on ZrO_2 and TiO_2 mesostructures, *RSC Adv.*, **3**, (2013) 18762-18766.
65. National Center for Photovoltaics, National Renewable Energy Laboratory (NREL) Website (www.nrel.gov/ncpv/)
66. G. F. Bryce, et al., 1-Histidine-containing peptides as models for the interaction of copper(II) and nickel(II) ions with sperm whale apomyoglobin, *J. Biol. Chem.*, **241**, (1966) 1072-1080.
67. S. L. Guthans, et al., The interaction of zinc, nickel and cadmium with serum albumin and histidine-rich glycoprotein assessed by equilibrium dialysis and immunoabsorbent chromatography, *Archives of Biochemistry and Biophysics*, **218**, (1982) 320-328.
68. N. Stock, et al., Synthesis of metal-organic frameworks (MOFs): Routes to various MOF topologies, morphologies, and composites, *Chem. Rev.*, **112**, (2012) 933-969.
69. J-P. Zhang, et al., Interweaving isomerism and isomerization of molecular chains, *Chem. Comm.*, **47**, (2011) 4156-4158.
70. H. Yang, et al., An unprecedented 3-D SHG MOF material of silver(I) induced by chiral triple helices, *Chem. Comm.*, **49**, (2013) 2909-2911.
71. Z-H. Li, et al., Two-dimensional copper-based metal-organic framework as a robust heterogeneous catalyst for the N-arylation of imidazole with arylboronic acids, *Inorg. Chem. Comm.*, **27**, (2013) 119-121.
72. P. Mahata, et al., The first observation of a Na_2TiS_2 related structure in 2-D anionic manganese trimesate intercalated by cationic imidazole, *Cryst. Eng. Comm.*, **11**, (2009) 560-563.

73. K. S. Park, et al., Exceptional chemical and thermal stability of zeolitic imidazolated frameworks, *P. Natl., Acad. Sci.*, **103**, (2006) 10186-10191.
74. L. Etgar, et al., Mesoscopic $\text{CH}_3\text{NH}_3\text{PbI}_3/\text{TiO}_2$ heterojunction solar cells, *J. Am. Chem. Soc.*, **134**, (2012) 17396-17399.
75. K. Tanaka, et al., Comparative study on the excitons in lead-halide-based perovskite-type crystals $\text{CH}_3\text{NH}_3\text{PbBr}_3$, $\text{CH}_3\text{NH}_3\text{PbI}_3$, *Solid State Commun.*, **127**, (2003) 619-623.
76. Y. Takahashi, et al., Charge-transport in tin-iodide perovskite $\text{CH}_3\text{NH}_3\text{SnI}_3$: origin of high conductivity, *Dalton Trans.*, **40**, (2011) 5563-5568.
77. E. Edri, et al., High open-circuit voltage solar cells based on organic-inorganic lead bromide perovskite, *J. Phys. Chem. Lett.*, **4**, (2011), 897-902.
78. J. H. Noh, et al., Chemical management for colorful, efficient, and stable inorganic-organic hybrid nanostructured solar cells, *Nano Lett.*, **13**, (2013) 1764-1769.
79. J-H. Im, et al., Synthesis, structure, and photovoltaic property of a nanocrystalline 2H perovskite-type novel sensitizer $(\text{CH}_3\text{CH}_2\text{NH}_3)\text{PbI}_3$, *Nanoscale Research Lett.*, **7**, (2012) 353-259.
80. T. M. Koh, et al., Formamidinium-containing metal-halide: An alternative material for near-IR absorption perovskite solar cells, *J. Phys. Chem. C.*, (2013) ASAP
81. R. W. Taft, et al., Electrostatic proximity effects in the relative basicities and acidities of pyrazole, imidazole, pyridazine, and pyrimidine, *J. Am. Chem. Soc.*, **108**, (1986) 3237-3239.
82. J. E. McMurry, Organic chemistry, 8th ed, Cengage Learning (2011)
83. T. Y. Miller, et al., A comparison between protein crystals grown with

- vapor diffusion methods in microgravity and protein crystals using a gel liquid-liquid diffusion ground-based method, *J. Cryst. Growth*, **122**, (1992) 306-309.
84. D. H. Kim, et al., Transmittance optimized Nb-doped TiO₂/Sn-doped In₂O₃ multilayered photoelectrodes for dye-sensitized solar cells, *Solar Energy Materials and Solar Cells*, **96**, (2012), 276-280.
85. H. Jiang, et al., Single-crystal growth of organic semiconductors, *MRS Bulletin*, **38**, (2013) 28-33.
86. N. Kitazawa, et al., Optical properties of natural quantum-well compounds (C₆H₅-C_nH_{2n}-NH₃)₂PbBr₄ (n = 1-4), *J. Phys. Chem. Solids*, **71**, (2010) 797-802.
87. J-P. Liu, et al, Ionothermal synthesis structure and optical properties of three new organic-inorganic hybrid imidazolium bromoplumbate complexes, *Inorg. Chem. Comm.*, **14**, (2011) 663-666.
88. Y. Li, et al., Synthesis, structure and optical properties of new organic-inorganic haloplumbates complexes (C₅H₁₀N₃)PbX₄ (X = Br, Cl), (C₂H₂N₄)PbBr₃, *J. Solid State Chem.*, **180**, (2007) 173-179.
89. Y. Y. Li, et al., Novel <110>-oriented organic-inorganic perovskite compound stabilized by N-(3-aminopropyl)imidazole with improved optical properties, *Chem. Mater.*, **18**, (2006) 3463-3469.
90. Y. Li, et al., Synthesis, structure and optical properties of different dimensional organic-inorganic perovskites, *Solid State Sci.*, **9**, (2007) 855-861.
91. U. Sim, et al., Nanostructural dependence of hydrogen production in silicon photocathodes, *J. Mater. Chem. A.*, **1**, (2013) 5414-5422.
92. H. Lin, et al., Size dependency of nanocrystalline TiO₂ on its optical property and photocatalytic reactivity exemplified by 2-chlorophenol, *Appl. Catal. B-Environ.*, **68**, (2006) 1-11.

93. W-J. Chun, et al., Conduction and valence band positions of Ta₂O₅, TaON, and Ta₃N₅ by UPS and electrochemical methods, *J. Phys. Chem. B.*, **107**, (2003) 1798-1803.
94. M. Sawicka, et al., TG-FTIR, DSC and quantum chemical studies of the thermal decomposition of quaternary methylammonium halides, *Chem. Phys.*, **324**, (2006) 425-437.
95. P. Mauersberger, et al., Structure of Cesium triiodostannate(II), *Acta Crystallogr. Sect. B*, **28**, (1972) 683-684.
96. J-Y. Jeng, CH₃NH₃PbI₃ perovskite/fullerene planar-heterojunction hybrid solar cells, *Adv. Mater.*, **25**, (2013) 3727-3732.
97. D. B. Mitzi, Thin-film deposition of organic-inorganic hybrid materials, *Chem. Mater.*, **13**, (2001) 3283-3298.
98. J. Burschka, et al., Sequential deposition as a route to high-performance perovskite-sensitized solar cells, *Nature*, **499**, (2013) 316-319.
99. J. F. Condeles, et al., Influence of solution rate and substrate temperature on the properties of lead iodide films deposited by spray pyrolysis, *J. Mater. Sci.*, **46**, (2011) 1462-1468.
100. J-H. Im, et al., 6.5% efficient perovskite quantum-dot-sensitized solar cell, *Nanoscale*, **3**, (2011) 4088-4093.
101. H-S. Kim, et al., High efficiency solid-state sensitized solar cell-based on submicrometer rutile TiO₂ nanorod and CH₃NH₃PbI₃ perovskite sensitizer, *Nano Lett.*, **13**, (2013) 2412-2417.
102. C. Ratsch, Nucleation theory and the early stages of thin film growth, *J. Vacuum Sci. & Tech.*, **21**, (2003) S96-S109.
103. K. R. Coffey, et al., Experimental evidence for nucleation during thin-film reactions, *Appl. Phys. Lett.*, **55**, (1989) 852.

국 문 초 록

유무기 페로브스카이트는 일반적인 무기 이온들로 구성된 페로브스카이트와 달리, 격자 내에 양전하를 갖는 유기 분자가 배치된 하이브리드 소재이다. 최근, 유무기 페로브스카이트가 고체 상 태양전지 내 감광제로 활용되며 효율이 기존보다 월등히 향상될 수 있음이 알려지면서 매우 많은 관심이 쏠리고 있다. 하지만 현재까지 대부분의 연구는 메틸암모늄 요오드화 납 기반의 감광제에만 국한되어 있으며, 해당 물질은 수분에 취약할 뿐만 아니라 단순한 일차 알킬 아민 분자를 사용한 구조이므로 다양한 변수를 통해 물질의 특성 변화를 유도하기 어렵다는 한계가 있다.

본 연구에서는, 생체 분자인 히스티딘과 히스타민을 이용하여 기존에 보고된 바 없는 새로운 형태의 이미다졸 기반 유무기 페로브스카이트를 최초로 합성하는 데 성공하였으며, 이를 고체 상 태양전지에 적용한 결과, 감광제 역할을 할 수 있는 신소재임을 밝혔다. 이와 더불어, 본 연구에서는 합성된 유무기 페로브스카이트의 구조 및 특성을 파악하기 위해 단결정 구조 분석, 밴드 구조 분석, 흡광 및 열 분석 등을 시도하였으며, 그 결과 합성된 물질의 결정 격자를 규명하고 밴드 구조를 밝히는 데 성공하였다. 이 후, 효과적인 태양전지 제작을 위해 코팅 방법을 크게 일 단계 스핀-코팅 방법과 두 단계 딥-코팅 방법으로 나누어 최적화된 조건을 찾아내었으며, 해당 조건을 이용해 태양전지를 제작하였다.

본 연구는 크게 세 가지 관점에서 의의가 있다. 첫째로, 기존 일차 알킬 아민에 국한된 유기 분자에서 탈피하여, 이미다졸 고리 자체가 페로브스카이트의 구조 내에 관여할 수 있음을 밝힘으로써 향후 다양한 유기물과 작용기 변화를 통해 특성 변화가 가능함을 보였다. 둘째로, 생체 유기분자가 관여된 새로운 하이브리드 소재를 제작함으로써 이미다졸 고리를 갖는 생체 재료와 무기 물질 간 새로운 융합의 접점을 제시하였다. 마지막으로, 기존 감광제보다 수분에 상대적으로 강한 내구성을 확인함으로써 유무기 페로브스카이트 고체 상 태양전지가 상용화 하는 데에 반드시 필요한 수분 안정성을 높일 수 있었다.

주요어: 유무기 페로브스카이트, 고체 상 태양 전지, 감광제, 이미다졸, 히스티딘, 히스타민, 단결정 구조 분석, 밴드 구조 분석, 한 단계 스핀-코팅 공정, 두 단계 딥-코팅 공정, 안정성

학 번: 2012 - 20644

